國立交通大學

機械工程學系

博 士 論 文

高液壓成型機台之研發與其在燃料電池上之應用

Studies on a novel high-pressure hydroforming apparatus and its

application in fuel cells

研 究 生：林志嘉

指導教授：洪景華　教授

中 華 民 國 一 零 二 年 七 月

高液壓成型機台之研發與其在燃料電池上之應用

Studies on a novel high-pressure hydroforming apparatus and its application in fuel cells

研 究 生：林志嘉　　　　　　　　　　Student：Chih-Chia Lin
指導教授：洪景華　　　　　　　　　　Advisor：Chinghua Hung

國 立 交 通 大 學
機 械 工 程 學 系
博 士 論 文

A Dissertation
Submitted to Department of Mechanical Engineering
College of Engineering
National Chiao Tung University
in partial Fulfillment of the Requirements
for the Degree of
Doctor of Philosophy
in
Mechanical Engineering

July 2013

Hsinchu, Taiwan

中華民國一零二年七月

高液壓成型機台之研發與其在燃料電池上之應用

研究生：林志嘉　　　　　　　　　　　　指導教授：洪景華 教授

國立交通大學機械工程學系

摘要

近年來隨著綠能科技崛起以及攜帶型 3C 產品需求增加，可攜式質子交換膜燃料電池逐漸受到矚目。而金屬材質的雙極板由於其具有低成本、優異的熱、電與機械性質以及能夠有較薄之厚度(0.1-0.5 mm)，因而成為了可攜式燃料電池中的主要零件。然而，以現有之成形技術仍無法在金屬薄板上有效成形出符合實際燃料電池所需具有高深寬比的流道結構。

本研究利用自行研發之高液壓成形機台，藉由提升成形製程中之成形壓力來達到提升微流道深寬比之目的。此設計包含了三個部分：一個能夠產生二段增壓的機械結構、一個能夠乘載高液壓的高壓承載筒，以及能夠將液壓密封的高壓密封元件。透過此研究，建立了一套完整的高液壓成形技術，並在現階段應用於可攜式燃料電池之金屬雙極板的製作上。

由實際實驗可知，此研發之高液壓成形機台不論在製程控制或是成形試片的重現性上均是合理且可接受的。在施加高達 250 MPa 之成形壓力下，其微流道之深寬比能夠達到 0.392，比傳統液壓成形所能得到之深寬比(0.31)提升了 26.5%。後續，再經過有限元素以及最佳化分析後，將可更有效率的利用此高液壓成形技術以獲得此成形機台的最佳成形能力，使成形試片上的微流道深寬比再提升4.8%。

關鍵詞: 燃料電池、高液壓成形機台、金屬雙極板、微流道、有限元素分析、最佳化分析

Studies on a novel high-pressure hydroforming apparatus and its application in fuel cells

Student: Chih-Chia Lin   Advisors: Dr. ChingHua Hung

Department of Mechanical Engineering

National Chiao Tung University

ABSTRACT

Portable proton exchange membrane fuel cells (PEMFCs) have received considerable attention recently because of the suitable material of the development of 3C production processes and green energy techniques. For the key component of portable PEMFCs, bipolar plates, metals such as stainless steel are becoming popular because of their excellent mechanical, electrical, and thermal properties, as well as a low degree of thickness (0.1–0.5 mm). However, current forming techniques cannot efficiently fabricate micro-flow-channels with a high aspect ratio on thin metallic blanks to satisfy the practical demands on portable fuel cells.

This study presents the development of a high-pressure hydroforming technique and explains the design and construction of an experimental high-pressure hydroforming apparatus. The apparatus is composed of a two-stage pressure-increase structure to provide high fluid pressure, a high-pressure container and high-pressure seals to maintain and seal the high fluid pressure. Conclusively, this research develops a complete high-pressure hydroforming technique and be applied in forming metallic bipolar plates for portable PEMFCs.

The results of our investigation indicate that the process control for the developed apparatus and the repeatability for hydroformed specimens are reasonably

acceptable. The aspect ratio of micro-flow channels formed using this apparatus can achieve 0.392 when a working pressure of 250 MPa is applied. Compared with the maximum channel aspect ratio of 0.31 formed using the traditional hydroforming process, the channel aspect ratio formed using the new technique and device is 26.5% higher. Furthermore, finite element and optimization analyses can be performed to boost the forming capability of the developed technique. Consequently, the aspect ratio of formed micro-flow channels can be further increased by 4.8%.

Keywords: Fuel cell; high-pressure hydroforming apparatus; metallic bipolar plate; micro-flow channels; finite element analysis; optimization analysis
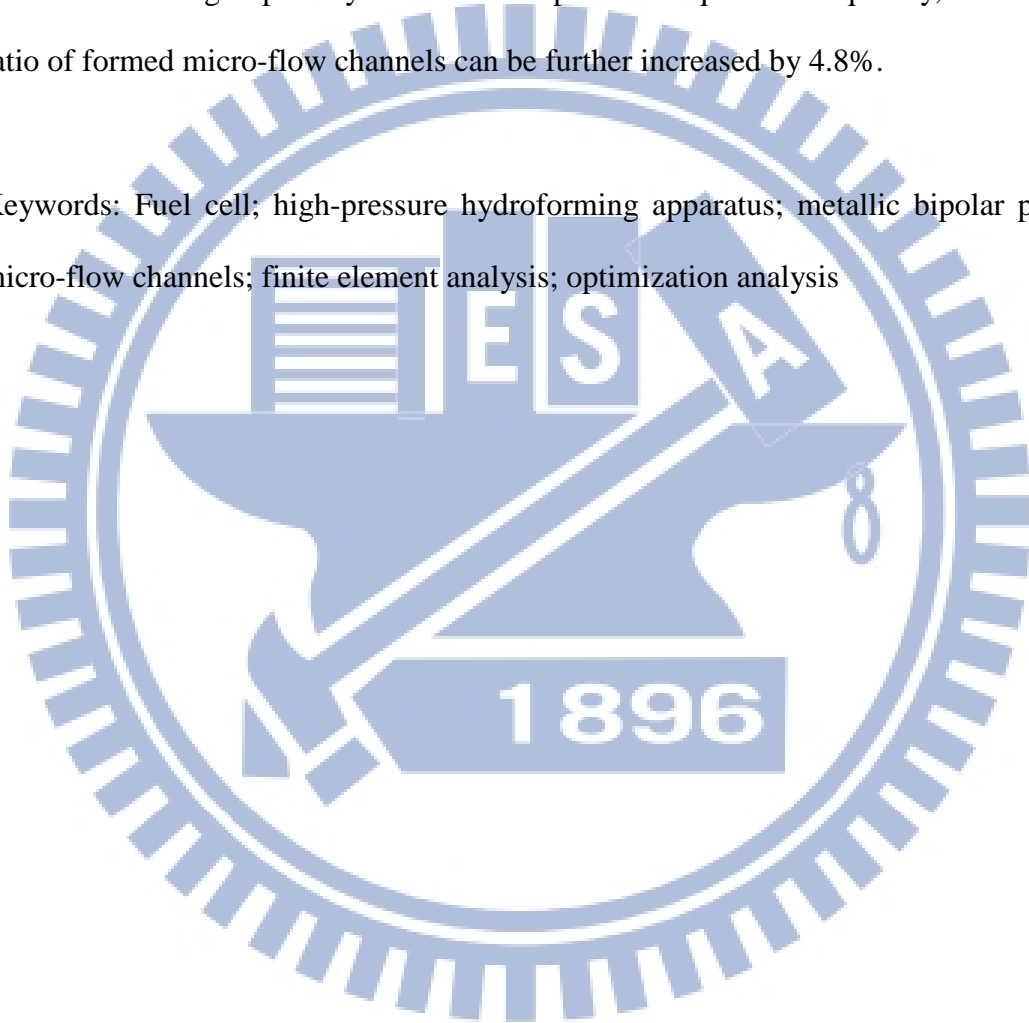
誌 謝

在這五年的博士生涯裡，首先，我要感謝的人是我的指導教授<u>洪景華</u>老師，在學業、研究方面的教導為學生指引了正確的方向，對於學生將來的生活很有幫助，謝謝老師不辭辛勞的指導。同時也感謝口試委員<u>宋震國</u>教授、<u>黃佑民</u>教授、<u>徐瑞坤</u>教授、<u>陳申岳</u>博士以及<u>洪榮崇</u>教授對於論文所提出的指正與建議。

感謝洪榮崇學長，在學長的指導以及帶領下才能夠讓我的博士論文得以順利完成;感謝宇中學長，實驗室在學長長期的帶領下備感溫馨;感謝麒禎學長，博學的知識，每每都能夠耐心解答我的疑惑;感謝彥彬學長，幽默風趣的言談讓實驗室時常充滿歡樂。還有感謝其他已畢業的博班學長，政成、正展、煌棊、岳儒、陽光、冠宇等等，在我求學階段對我的照顧。

感謝其他實驗室的夥伴們:安靜的銘傑學長、搞笑的志傑、幽默的明輝學長、激動的璟璿、害羞的蘭芳、憨厚的俊元、rock的毅恆、古錐的文玉、很有女人緣的榆文、只吃巧克力的正斌、裝酷的祺津、強壯的東佑、可愛的宛伶、十字胸毛的逸翔，回到大陸的阿岳，剛進實驗室的佑傑、瑋倫、名惠以及八寶粥，還有理強、宗駿、黃詠、世璿、運賢、俊羿、聖平、時恆、建榮、麒翔、忠諭、宗錞、筱偉、立釗、正一、振傑、雅喬、中南、書麟、馨匀、宜均、呂翔、致豪、品帆、彥佑，在我的求學階段由於你們各位的出現，讓研究不再枯燥，讓求學階段充滿了美好的回憶。

此外，我要特別感謝我的爸爸、媽媽、弟弟以及我的女友未來的老婆<u>千儀</u>，在我學習的過程中在背後默默的支持鼓勵我，讓我無後顧之憂的打拼學業。

在實驗室待久了，經歷過了無數次的分離。天下無不散的筵席，這次輪到我離開了，離開待了 11 年的地方，珍重!

<div style="text-align: right">

林志嘉　謹誌

</div>

TABLE OF CONTENTS

LIST OF TABLE

LIST OF FIGURE

CHAPTER 1 INTRODUCTION

1.1 Research background

The current high price of oil is largely due to increases in the price of crude oil and the growing economies of Asian nations. Because of these high prices, as well as variations in the global climate, finding high-efficiency replacement energy sources is one of the most critical issues affecting the world today.

Fuel cells are devices that can generate energy without burning fuel and have high efficiency, quiet operation, and near-zero pollution [1-6]. The following five main categories of fuel cells are listed in the order of their operating temperature:

1) Proton exchange membrane or polymer electrolyte fuel cell (PEMFC, PEFC);

2) Alkaline fuel cell (AFC);

3) Phosphoric acid fuel cell (PAFC);

4) Molten carbonate fuel cell (MCFC);

5) Solid oxide fuel cell (SOFC).

PEMFC and SOFC use a solid phase membrane as the cell separator and electrolyte. The other three use liquid electrolytes. Regarding sealing, assembly, and handling, using solid membranes is less complex than using other types of fuel cell systems. Table 1.1 [7] provides a summary of the major differences of fuel cell types.

Table 1.1: Major differences of fuel cell types [7].

	PEMFC	AFC	PAFC	MCFC	SOFC
Operating Temperature	60-100°C	65-260°C	150-210°C	600-1000°C	600-1000°C
Electrolyte	Ion Exchange Membranes	Mobilized or Immobilized Potassium Hydroxide	Immobilized Liquid Phosphoric Acid	Immobilized liquid Molten Carbonate	Ceramic
Charge Carrier	H+	OH-	H+	CO_3^{-2}	O-2
External Reformer for CH4	Yes	Yes	Yes	No	No
Catalyst	Platinum	Platinum	Platinum	Nickel	Perovskites
Prime Cell Components	Carbon-based	Carbon-based	Graphite-based	Stainless-based	Ceramic
Product Water Management	Evaporative	Evaporative	Evaporative	Gaseous Product	Gaseous Product
Gaseous/Liquid Water formation	Cathode	Anode	Cathode	Anode	Anode
Fuel	Pure H2 (tolerates CO2)	Pure H2	Pure H2 (tolerates CO2, 1.5% CO)	H2, CO, CH4, other hydrocarbons (tolerates CO2)	H2, CO, CH4, other hydrocarbon (tolerates CO2)
Electrical Efficiency	40-60%	60-70%	36-42%	50-60%	50-60%

PEMFC and SOFC have received considerable attention because of their simpler systems. SOFC belongs to a high-temperature fuel cell (600–1000 °C), which is suitable for use in a power plant. PEMFC, by contrast, belongs to a low-temperature fuel cell (60–100°C) and can vary output quickly to meet shifts in power demands. Therefore, PEMFC is suited to transportation applications that require quick startups. PEMFCs can also be used in light-duty vehicles, buildings, and smaller applications such as replacements for rechargeable batteries.

The critical component of the PEMFC consists of two electrodes, the anode and the cathode, separated by a polymer membrane electrolyte. Figure 1.1 shows the basic operating principle of PEMFC. An electrolyte layer (the proton exchange membrane) makes contact with the porous anode and cathode on both sides. Bipolar plates with channels are located outside the electrodes. Through these channels, hydrogen and oxygen are continuously introduced into the anode and cathode, respectively, and the oxidation-reduction reaction occurs on the electrodes. A proton arrives at the cathode

through the electrolyte layer, and an electron from the anode reaches the cathode along an outer circuit. Finally, energy is generated with some water and heat. Furthermore, the heat-recycle design can be used to promote the ratio of energy utilization up to 70%, which is greater than that of oil at 30–40%.

Anode reaction: $H_2 \rightarrow 2H^+ + 2e^-$

Cathode reaction: $\frac{1}{2}O_2 + 2H^+ + 2e^- \rightarrow H_2O$

Combined reaction: $H_2 + \frac{1}{2}O_2 \rightarrow H_2O$
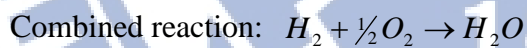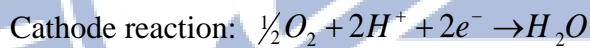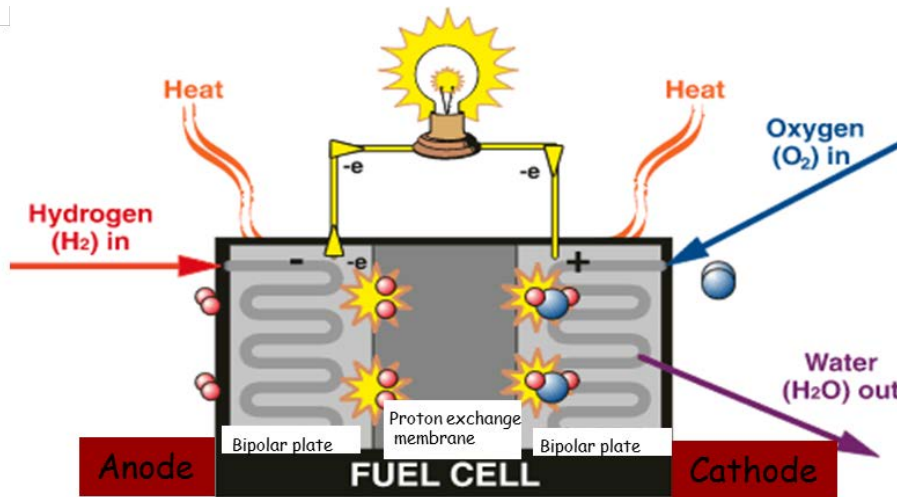
Figure 1.1: Schematic representation of a PEMFC operation principle [8].

Despite the proven advantages of fuel cells, they are not yet cost-competitive when compared to existing power generation technologies. This is especially true in transportation applications. For conventional PEMFCs, bipolar plates compose nearly 60–80% of the stack weight, 50% of the stack volume, and 35–45% of the stack cost [1, 9-10]. Bipolar plates are usually made of graphite (see Figure 1.2a), a material that is difficult to handle due to its low mechanical strength and brittleness, causing the formation of flow channels in graphite to be a challenging, and expensive process, especially for portable PEMFCs.

By contrast, metallic bipolar plates (see Figure 1.2b) are estimated at 15–30 % of the stack of fuel cell costs compared to graphite [1, 11]. Metallic plates also have excellent mechanical, electrical, and thermal properties, as well as a low degree of thickness (0.1–0.5 mm). Therefore, metallic bipolar plates offer advantages for PEMFCs and, in particular, for portable PEMFCs, replacing graphite bipolar plates in the near future.
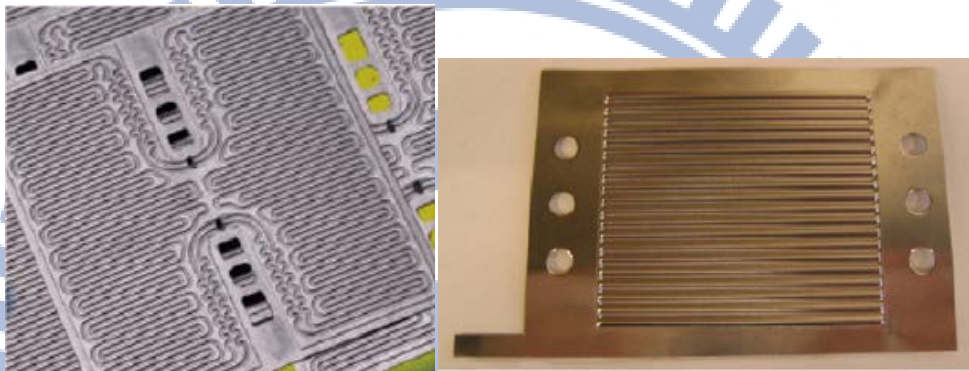
Figure 1.2: (a) Graphite and (b) metallic bipolar plates [1].

With the popularity of portable 3C productions, the demand for portable rechargeable devices has increased. Portable PEMFCs with metallic bipolar plates have thus been developed. However, with reducing the sizes of PEMFCs, keys to developing portable PEMFCs are cell performances and micro-fabrication technique for micro channels on metallic bipolar plates

1.2 Literature review

1.2.1 Effect of bipolar plate micro channels on cell performance

Manso [12] investigated the influence of the channel aspect ratio, defined as the ratio of the channel height to the width, d/W, on the performance of a PEMFC with a serpentine flow field design (see Figure 1.3). The results indicated that the cell performance improved as the channel aspect ratio increased at high operating voltages,

where the influence of mass transporting velocity was predominant. Our previous research [13] also revealed that the performance of portable PEMFCs with metallic bipolar plates can be improved if the aspect ratio of micro-flow channels is higher.

	Range
d	0.27-4 mm
W	0.27-4 mm
d/W	0.07-15
$d \times W$	1.06 mm^2
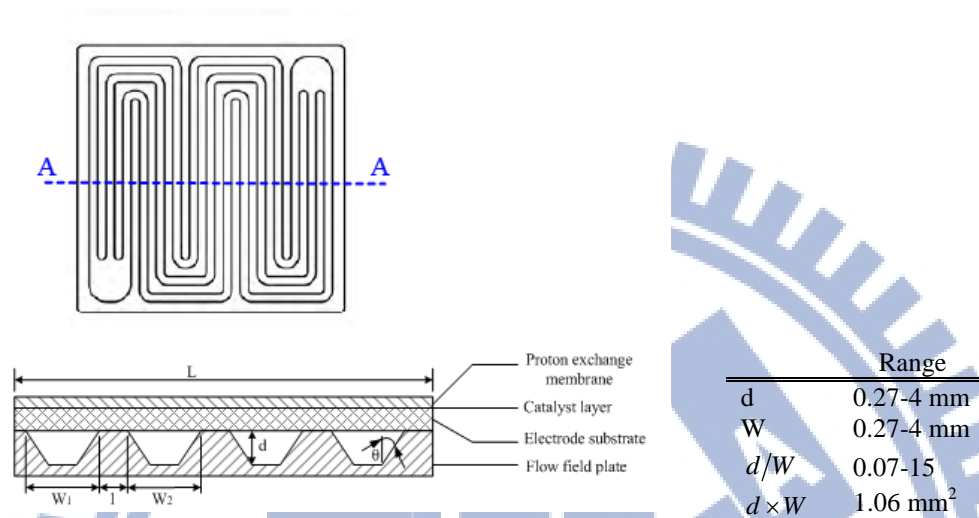
Figure 1.3: Schematic representation of a PEMFC structure [12].

1.2.2 Forming techniques of micro channels on metallic bipolar plates

Current manufacturing methods of metallic bipolar plates include electrochemical micro-machining processes [14], rubber pad forming processes [15-16], stamping processes [17], and hydroforming processes [1, 17-18]. Among these processes, electrochemical micro-machining resulted in poor surface quality on formed parts. This method was, therefore, inefficient. Likewise, the rubber pad forming process was limited by the fluidity of the rubber pad. And the conventional stamping technique was limited by the apparatus because the supplied force was not uniform. Although this technique had the fastest forming velocity thereby reducing the stack cost, the used specimen did not obtain a high precision profile.

To offer uniform pressure from the stamping apparatus, Masatoshi et al. [19] added a stress buffer layer between the apparatus and the upper die. Olsson et al. [20]

added a chamber that injected the fluid inside and between the apparatus and the upper die (see Figure 1.4).
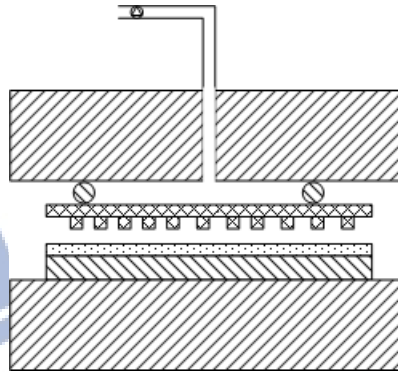
Figure 1.4: Schematic of Olsson's stamping apparatus design [20].

During the stamping process, it is difficult for the specimens and dies to make perfect contact because of their surface roughness. This also affects the material fluidity inside the apparatus. Lee et al. [21] changed the lower die into an inflatable pipe to ensure more effective contact between the specimens and dies, which also improved the uniformity of contact pressure (see Figure 1.5).

(a)   (b)
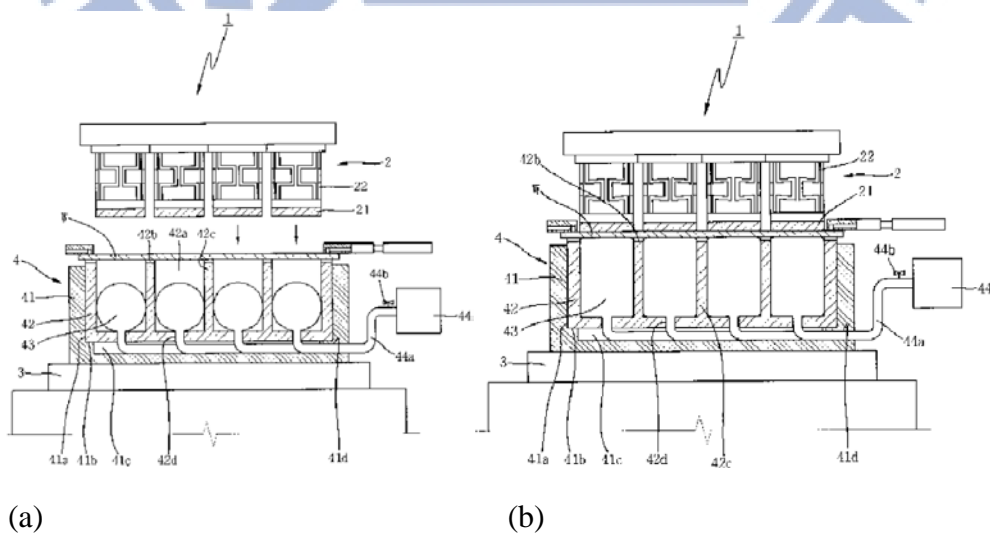
Figure 1.5: Schematic of Lee's stamping apparatus design [21]. (a) Before and (b) during the process.

Ando [22] proposed the hydroforming technique, another micro structure impress technique, and the specimen that resulted was formed by pressurized fluid used as an isotropic working medium. The uniform pressure can be supplied by pressurized fluid, and the micro-structure of the mold can be impressed on the specimen more uniformly (see Figure 1.6).
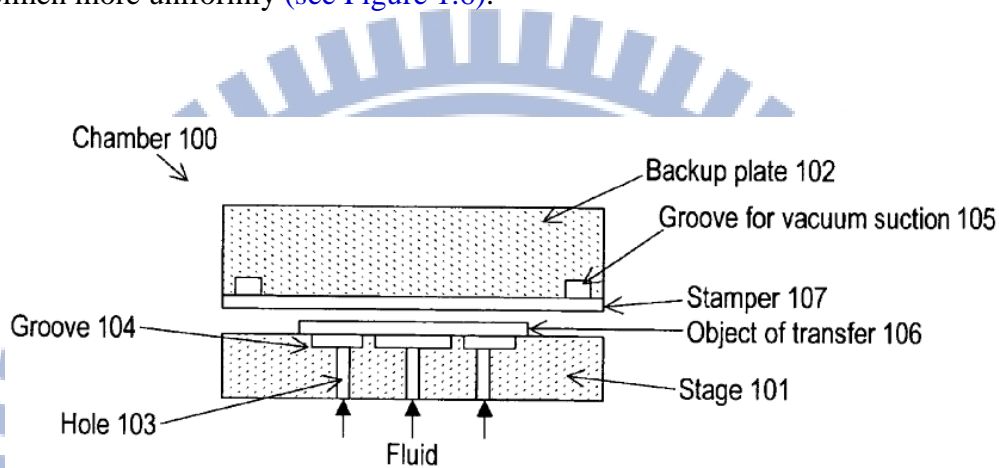
Figure 1.6: Schematic of Ando's hydroforming apparatus design [22].

Mahabunphachai et al. [17] compared hydroforming and stamping processes and formed 26 parallel micro-channels on 0.051-mm-thick stainless steel 304 sheets (SUS304) with a yield strength of 215 MPa. The results indicated that the maximum in-plate height variation of the stamping process was 4.1% higher than that of the hydroforming process, which was 1.3%. The aspect ratio of micro-flow channels formed by the hydroforming process was 0.31, which was higher than that of the stamping process with an aspect ratio of 0.26. A literature review showed that specimens formed by the hydroforming process exhibited superior uniformity, repeatability, and aspect ratio compared to those formed by the stamping process. Furthermore, during the hydroforming process, no friction was observed between the high-pressure fluid and the specimen, thus reducing the friction force effect on the

process and resulting in an optimal surface roughness for the specimens after the hydroforming process.

Koc and Mahabunphachai [1, 18] have used the hydroforming process to produce micro-flow channels of various dimensions on 0.051-mm-thick SUS304 plates using pressures of 55.2 MPa and 82.7 MPa. The results indicated that the aspect ratios of micro-flow channels formed at 55.2 and 82.7 MPa may reach approximately 0.26 and 0.29, respectively. The research also demonstrated that it was necessary to choose a larger rib and channel width, fewer flow channels, and higher fluid pressure to obtain a high aspect ratio and excellent formability. Furthermore, Mahabunphachai [18] also used finite element software to simulate the hydroforming process. The results revealed that it was necessary for the hydrostatic pressure to reach 843 MPa to form micro-flow channels with a high aspect ratio of 0.72.

1.3 Motivation and objective

Based on the reviewed literature, fuel cell performance can be improved by increasing the aspect ratio of micro-flow channels. However, previous research on the hydroforming process applied in forming metallic bipolar plates was limited to a hydrostatic pressure of 82.7 MPa on 0.051-mm-thick metallic plates with a maximum aspect ratio of 0.31, which cannot satisfy practical demands for cell performance or reveal the forming capability of the hydroforming process. Nevertheless, problems remain with respect to building high-pressure hydroforming devices, and only a few studies on high-pressure hydroforming techniques have been published.

To improve formability and produce micro-flow channels with a high aspect ratio, this study increased the forming pressure during the hydroforming process. For this purpose, a novel high-pressure hydroforming testing apparatus was developed. In addition, finite element and optimization analyses were performed to further reveal

the forming capability of the developed technique.

Conclusively, this research developed a complete high-pressure hydroforming technique, applied in forming metallic bipolar plates for portable PEMFCs.

1.4 Research method

A novel patented apparatus [23] was first designed and constructed to enable a two-stage pressure boost in the hydroforming process. It was designed to have a working pressure that reaches 1000 MPa. A high-pressure container was designed with three-layered tapered cylinders to sustain maximum working pressures over 1000 MPa. In addition, a special seal component was designed to seal the high-pressure fluid and, thus, maintain pressure. A series of preliminary tests were subsequently conducted to verify the feasibility of this high-pressure hydroforming technique and to ensure that all of the components in the hydroforming apparatus worked smoothly. Finally, the hydroforming experiments were conducted using various hydrostatic pressures to form high aspect ratio micro-flow channels on stainless steel sheets. A fuel cell performance test was also performed to check the performance of hydroformed metallic bipolar plates.

Concurrently, finite element analysis software was used to analyze the hydroforming process. First, the precision of the finite element model was verified by comparing the results between simulations and experiments. Subsequently, the optimization software was implemented into the finite element software to determine the optimal aspect ratio of micro-flow channels by changing the dimension of micro-flow channels on the mold.

This study used SUS304 as the material for metallic bipolar plates to overcome the corrosion problem in working environments [1, 24-28]. Although different types of stainless steel (e.g., SUS304, SUS316, SUS316L, SUS317L, SUS904L, and

SUS349) could be used as a base material for bipolar plates, SUS304 was selected in this research for its low material cost, acceptable corrosion resistance, and availability [29]. Moreover, 0.051-mm-thick SUS304 plates used in previous studies [1, 17-18] were not sufficiently thick to meet practical demands on rigidity; therefore, 0.1-mm-thick SUS304 plates were used as the specimens in this research.

1.5 Scope of dissertation

This chapter introduces the background of bipolar plates in fuel cells and the high-pressure hydroforming process, thus revealing the motivation and objectives of this research. Chapter 2 describes the detailed designs and structure of the newly developed high-pressure hydroforming apparatus. In Chapter 3, a series of preliminary experiments using the constructed hydroforming apparatus are conducted to verify the feasibility of the proposed high-pressure hydroforming technique. In Chapter 4, the precise finite element and optimization analyses are conducted to efficiently reveal the full capability of this developed apparatus. Chapter 5 summarizes the study and draws conclusions.

CHAPTER 2 THE DESIGN AND CONSTRUCTION ON A HIGH-PRESSURE HYDROFORMING APPARATUS

Traditional hydroforming processes (see Figure 2.1) [1, 17-18] formed the micro-flow channels with the forming pressure generated directly by a hydraulic pump and adopted copper gaskets as seal component; therefore, the forming pressure was limited by the power of the pump. Furthermore, the traditional pressure container with a single layer construction could not sustain the ultra-high pressure, and posed an fracture risk.
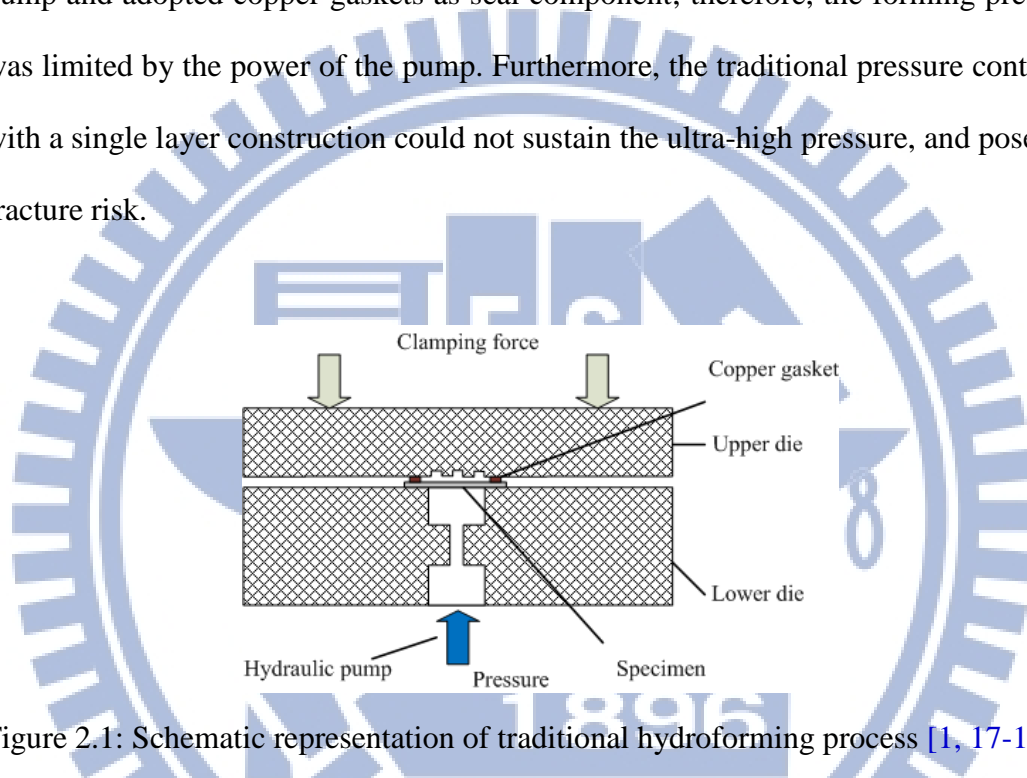
Figure 2.1: Schematic representation of traditional hydroforming process [1, 17-18].

2.1 High-pressure source

To increase the forming pressure, a novel mechanical structure was designed and constructed to enable a two-stage pressure increase in the apparatus (see Figure 2.2). According to our previous research [30], the high pressure of this experimental hydroforming apparatus is created by compressed fluid in a high-pressure container. This cylindrical high-pressure container has an inner bore 60 mm in diameter fitted to the secondary plunger. When a servo hydrostatic pressing machine with a maximum capacity of 100 tons, the design of which was attached in Appendix A, is used to

compress the fluid in the pressure container through the primary plunger, the secondary plunger is pushed, and a magnified fluid pressure as high as 1000 MPa (approximately 10,000 atm pressure) is obtained in the high-pressure container.
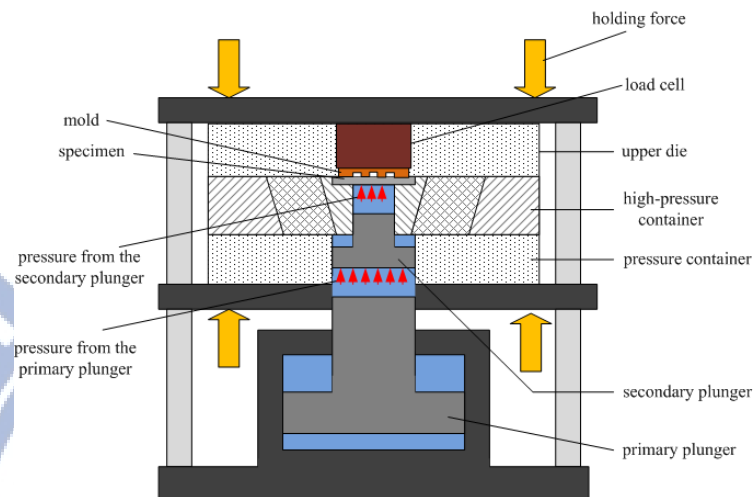
Figure 2.2: Schematic representation of a high-pressure source.

2.2 High-pressure container

The high-pressure container was designed and constructed to sustain the ultra-high hydrostatic pressure. Numerous problems were considered, such as material yielding, and seal design. According to Lame's equation for thick wall cylinders [31], the maximum stress at the internal wall of the high-pressure container reaches 1900 MPa when an internal pressure of 1000 MPa is applied. Very expensive and rare metal such as maraging steels is required if a single-layered cylinder is designed for the high-pressure container. Consequently, according to the multi-layer cylinders theory which utilizes the tight fit between cylinders to generate the residual stress to resist the internal pressure, a three-layered cylindrical container (see Figure 2.2) was adopted as the high-pressure container in this design, and the chosen material of each cylinder was SKD61 tool steel, which is economically and commercially available

[30].

The yield stress for SKD61 was approximately 1600 MPa. With a safety factor of 1.5, as indicated in the literature [30], 1060 MPa was specified as the design working stress (σ_y) during the design phase.

The Tresca yield criterion was often used to analyze a compound cylinder in multi-layer cylinders theory [32-36]. Based on the Tresca yield criterion, the pressure difference across an nth element at yield at the bore of the element is calculated as follows:

$$P_n - P_{n+1} = \frac{\sigma_{yn}}{2}(1 - \frac{1}{K_n^2}) \qquad (1)$$

where σ_{yn} is the specified working stress of the material for each element, and K_n is the diameter ratio of each cylinder. If m elements and no external pressure on the outer element occur, that is, $P_{m+1} = 0$, the internal pressure to produce simultaneous yielding in all cylinders is calculated as follows:

$$P_y = \sum_{n=1}^{m} \frac{\sigma_{yn}}{2}(1 - \frac{1}{K_n^2}) \qquad (2)$$

The maximum value of P_y is determined by differentiating (2) regarding K_n and equating to 0. Three elements were used in this study, and the material of each cylinder was the same. Equation (2) becomes

$$\frac{P_{y\max}}{\sigma_y} = \frac{3}{2}(1 - \frac{1}{K_t^{2/3}}) \qquad (3)$$

where σ_y is 1060 MPa, K_t is $K_1 \times K_2 \times K_3$, K_1, K_2, and K_3 are the diameter ratios of the inner cylinder, the middle cylinder, and the outer cylinder respectively.

Because of limitations on the dimension of the apparatus and requirements for

fuel cells, the designed diameters for the bore of the internal cylinder and the outer diameter of the outer cylinder were 60 mm and 500 mm, respectively, for this experimental hydroforming apparatus, and subsequently, $K_1 = K_2 = K_3 = 2.027$. The upper limit to this analysis occurs when the compressive residual stress at the bore of the inner cylinder, which is caused by the shrinkage stress produced by adding an outer element, exceeds the yield strength of the material. Furthermore, in this design, $P_{y\max}$ was up to 1203.17 MPa, which should be able to sustain a high-pressure fluid higher than 1000 MPa.

Owe to the ideal theoretical design, there were some hypotheses in the design. The residual stress between each cylinder generated from the tight fit, for example, is set as high as yield stress of cylinder material. Therefore, finite element analysis (Abaqus/Standard) for the high-pressure container was conducted first to verify the feasibility of the design for the high-pressure hydroforming apparatus. Three steps were performed as follows: the first step was to simulate the fitting of the middle cylinder into the outer cylinder. The second step was to simulate the fitting of the internal cylinder into the middle cylinder. The final step was to simulate the condition when a high pressure with a magnitude of 1000 MPa was applied to the inner surface of the three-layered high-pressure container. The final von Mises stress contour (see Figure 2.3) indicated that the highest stress of 990 MPa in the inner surface of the high-pressure container was lower than the working strength of the container material (1060 MPa), which verified the feasibility of a theoretical design of the high-pressure container.
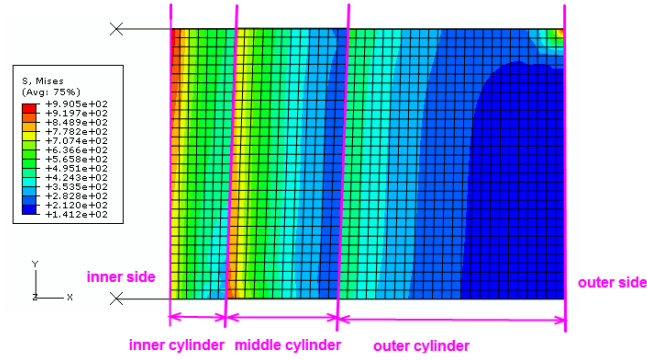
Figure 2.3: The final von Mises stress contour in the finite-element simulation of the high-pressure container. (Unit: MPa)

Tapered cylinders with a small taper angle of 2° were chosen and a substantial axial force of approximately 700 tons was required to fit the tapered cylinders into each other. After fitting, a surface polishing process was performed on the high-pressure container (see Figures 2.4a and 2.4b).
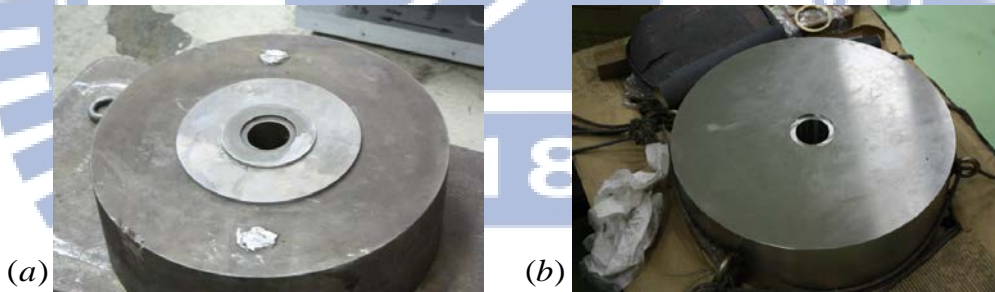
Figure 2.4: Three-layer tapered cylinder (a) before and (b) after fitting and surface polishing.

2.3 High-pressure seal component

The high-pressure seal component was required to seal the high-pressure fluid and maintain the high pressure. Bridgman et al. [37] first proposed a high-pressure seal consists of an O-ring backed by a metal backup ring to prevent leakage under high pressure. The cross section of this metal backup ring is quadrilateral, the

15

so-called unsupported-area-ring or Mitre ring; however, the friction between the O-ring and the metal backup ring increases in conjunction with the pressure, resulting in an additional torsion moment [30]. To overcome this problem, Whalley [38] and our previous research [23, 30] developed a ladder-shaped and a V-shaped cross-section ring, respectively.

To prevent leakage caused by the high pressure, the seal used for this hydroforming apparatus was an O-ring, which is characterized as P series and can be used in pressures up to 21 MPa, with a V-shaped metal backup ring made of beryllium copper, which has a hardness of HRC40 and yield strength of 1172 MPa (see Figure 2.5a). The inclined plane of the backup-ring was tightly fitted onto the O-ring, and thus, prevented the O-ring from being extremely squeezed into the gap between the specimen and the high-pressure container (see Figure 2.5b). These high-pressure seal components were positioned at each interface of parts in the apparatus to prevent leakage (see Figure 2.6).
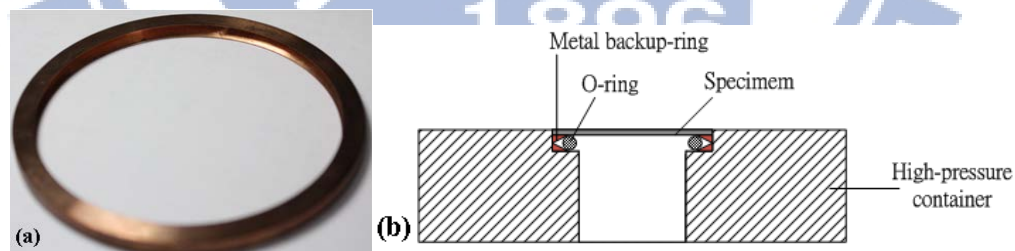
Figure 2.5: (a) The metal backup-ring and (b) schematic representation for the assembly of the high-pressure seal and the high-pressure container.
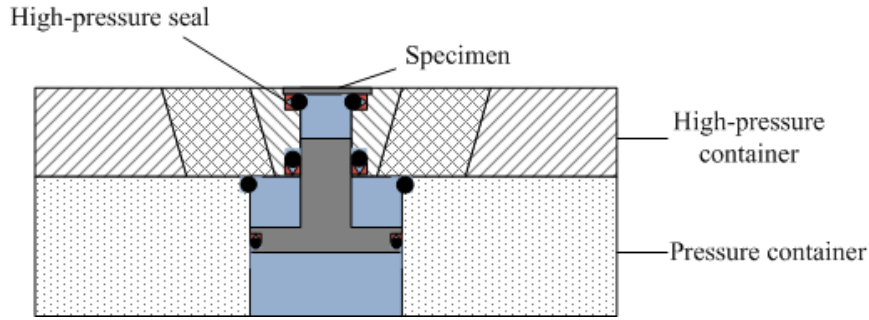
Figure 2.6: Schematic of the position of each high-pressure seal component in the apparatus.

2.4 High-pressure plunger (secondary plunger)

The functions of the high-pressure plunger are both to seal the container and to build the pressure. When the plunger is forced into the container, the pressure of the compressed fluid will increase and then deform the specimens. During the hydroforming process, the working pressure of 1000 MPa will be generated from the apparatus, and the plunger will sustain a great axial force that might cause buckling. Therefore, the clause No. 1.5.13 of the American Institute of steel construction (AICS) was adhered for the design of this plunger. Basically, AICS stipulates the allowance of compressive stress for taking axial force (see Figure 2.7), where the upper limit on the elastic bulking is half of material yield stress. Moreover, the slenderness ratio, a design boundary point between elastic and plastic bulking, is calculated as follows:

$$C_C = \sqrt{\frac{2\pi^2 E}{F_y}} \qquad (4)$$

where E and F_y are Young's Module and yield stress of material.
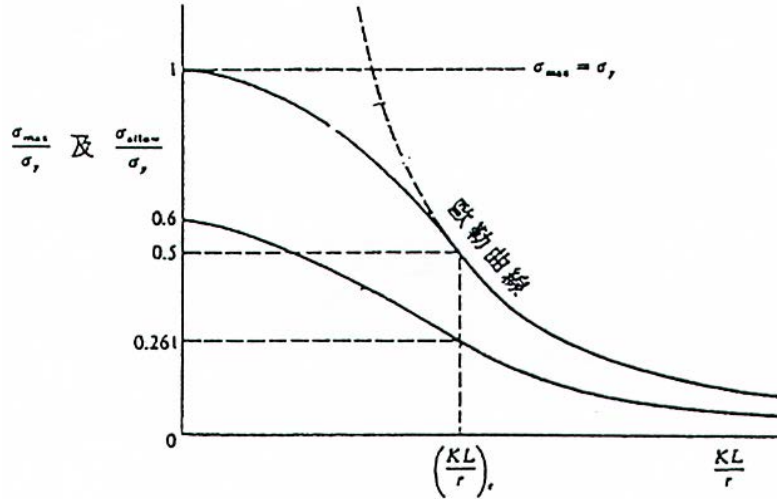
Figure 2.7: Design formula figure for a steel-structure pillar. (Received from J. M. Gere ＆ Timoshenko. 1990)

When $C_c > \dfrac{k \cdot L}{r}$, the plastic bulking design will be utilized, and k is the ideal design parameter, L is the length of the plunger, and r is the radius of the plunger. The standard design of plastic bulking is calculated as follows:

$$\sigma_a = \frac{\left[1 - 0.5 \times \left(\dfrac{\frac{k \cdot L}{r}}{C_c}\right)^2\right] \times F_y}{\dfrac{5}{3} + \dfrac{3 \times \left(\dfrac{k \cdot L}{r}\right)^2}{8C_c^2} - \dfrac{\left(\dfrac{k \cdot L}{r}\right)^3}{8C_c^3}} \qquad (5)$$

where σ_a is the allowance of compressive stress.

According to the allowance of compressive stress obtained by previous formula, the material selected for the high-pressure plunger was SKD61 tool steel, which has yield stress of 1600 MPa. After computing the slenderness ratio and the geometrical parameters according to AICS, it was found that plastic-buckling criterion should be used for the design.

The front section of the plunger has a diameter of 60 mm, and a high-pressure

seal with an O-ring and a beryllium copper backup is fitted on the plunger (see Figures. 2.8a and 2.8b).

(a) (b)
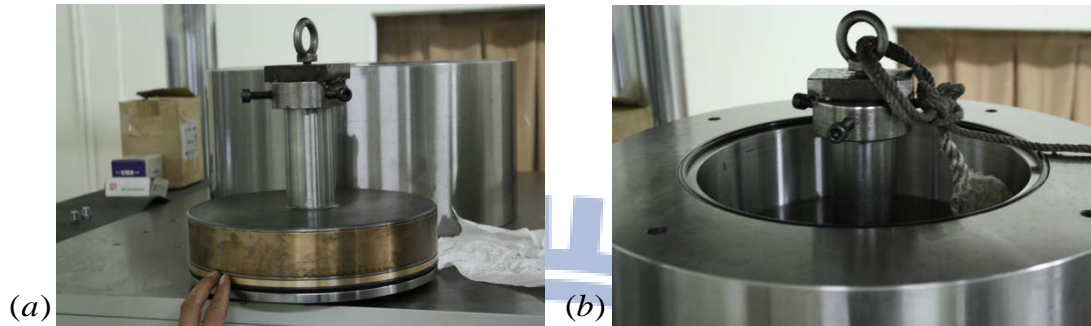
Figure 2.8: (a) The secondary plunger. (b) The secondary plunger in the pressure container.

2.5 High-pressure fluid

The fluid in the pressure containers has two functions, that is, to transmit pressure and to lubricate the interface between the plunger and the container. The fluid must be incompressible and safe under high pressure, and have excellent lubrication and stability.

Circulation oil R68, SAE30 oil, mineral oil, castor oil, and glycerine are commonly utilized. SAE30 oil can sustain pressure of 1000 MPa, R68 and castor oil can sustain 1500 MPa working pressures, and glycerine can sustain up to 3000 MPa working pressures; however, R68 is relatively cheap and commercially available. Hence, this study chose circulation R68 oil from Chinese Petroleum Corp. as the pressure fluid.

CHAPTER 3 EXPERIMENTAL INVESTIGATIONS OF THE HIGH-PRESSURE HYDROFORMING TECHNIQUE

This research did a series of preliminary experiments using the constructed hydroforming apparatus to verify the feasibility of the proposed high-pressure hydroforming technique. Moreover, a fuel cell with a pair of hydroformed bipolar plates was assembled to test its performance and to confirm the feasibility of hydroformed bipolar plates.

3.1 Material test

Before the high-pressure hydroforming experiments, the material properties of the specimen (SUS304) should be overall understood. Thus, the uniaxial tensile tests for specimens were conducted. In addition, metallographic test and forming limit test were also conducted in this research to comprehensively obtain the material properties of SUS304, the experiment results of which were attached in Appendix B and C.

3.1.1 Solution heat treatment

Thin SS304 blanks with dimensions of 100 mm × 100 mm × 0.1 mm were used as specimens for the hydroforming experiments. The uniaxial tensile test was conducted for SUS304 specimens before the heat treatment once, and the result (see Figure 3.1) shows that a yield stress of SUS304 specimens was extremely higher than that shown in material's textbook because of the working hardening effect on the specimens. Therefore, all the specimens received the solution heat treatment to remove work hardening histories and make these specimens act as a benchmark.
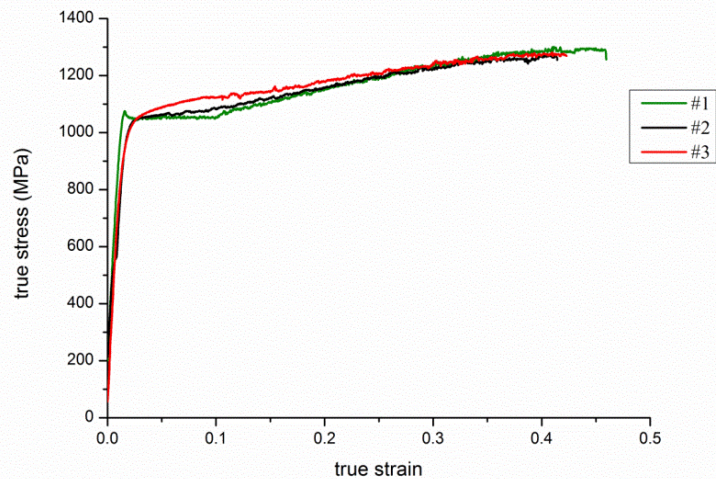
Figure 3.1: Stress-strain curve derived from SUS304 specimens before the solution
heat treatment.

SUS304 is a kind of austenitic steel having recrystallization temperature of 850 –
1000 °C and melting point of about 1400 °C. Therefore, the temperature of the
solution heat treatment needs to reach between 1000 °C and 1400 °C. In this research,
the temperature was set as 1030 °C. The procedure of the solution heat treatment is as
follows (see Figure 3.2): First, the temperature reaches 600 °C from room
temperature with a heating rate of 10 °C per minute, and then the temperature is held
for 30 minutes to make sure the temperature in a chamber is uniformly distributed.
Subsequently, the temperature is raised to 850 °C and held for 30 minutes. The
purpose of this raised temperature stage is to avoid the sensitizing temperature of
SUS304 stainless steel. Chromium carbide (Cr_3C_2) is precipitated in SUS304
specimens at approximately 600 °C. Finally, the temperature is raised to 1030 °C and
held for 2 hours, then cooled down slowly by nitrogen. Figure 3.3 is a comparison of
SUS304 specimens before and after the solution heat treatment.
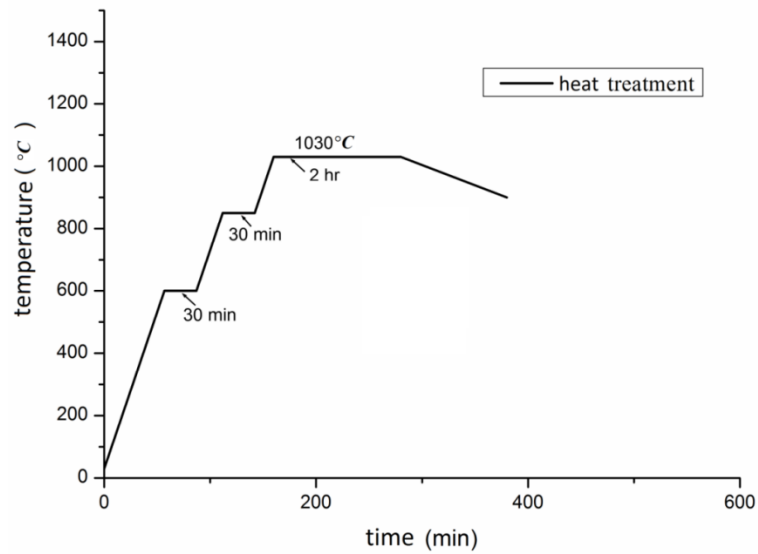
Figure 3.2: The procedure of the solution heat treatment.

(*a*)　　　　　　　　　　　　　　　　(*b*)
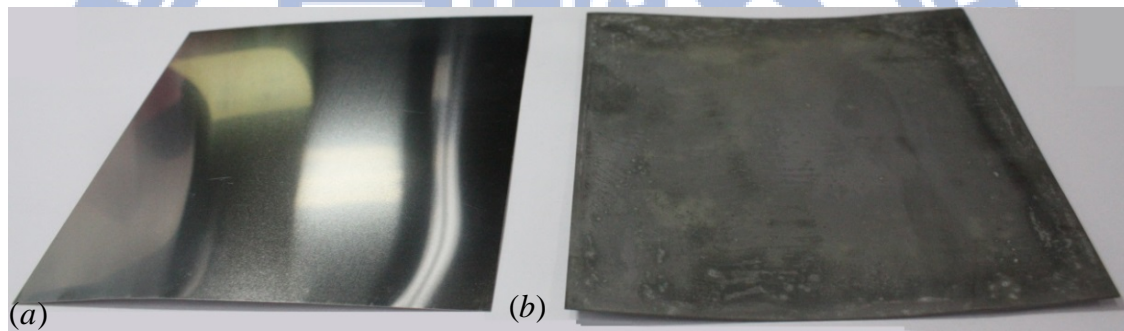
Figure 3.3: A comparison of SUS304 specimens (a) before and (b) after the solution

heat treatment.

3.1.2 Uniaxial tensile test

The purpose of the uniaxial tensile test is to obtain the basic mechanical properties such as Young's Module, yield stress, plastic data, and orientation, which also will be applied in the material properties of the finite element analysis.

Heat treated SUS304 specimens were cut to the standard tensile specimens (see Figure 3.4) according to No. ASTM-E8 of the American Society for Testing and Materials (ASTM). Furthermore, to consider the anisotropy effect, the samples at the same sheet were cut in the directions of 0°, 45° and 90° with respect to the rolling

direction, as shown in Figure 3.5. The tensile tests were carried out using MTS-810 universal testing machine equipped at room temperature. During the test, tensile rate was set as 0.025 mm s^{-1}, and the force, displacement, and strain could be obtained from the load cell and the strain gauge, respectively. Finally, the true stress-strain curve was derived by those data.
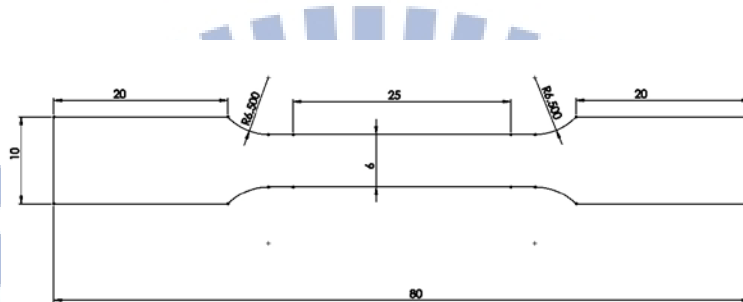
Figure 3.4: The dimension of the standard specimen for a tensile test. (Unit: mm)
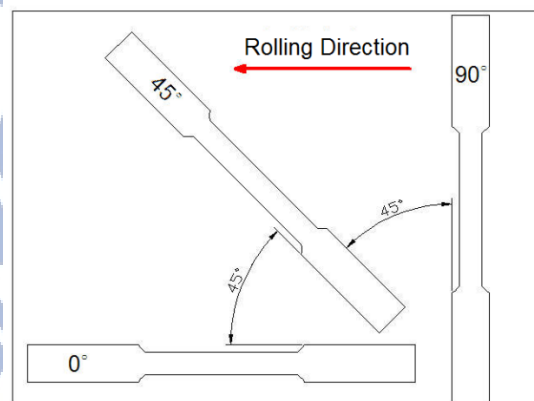
Figure 3.5: The layout of the standard specimens for a tensile test.

The heat treated specimens after the tensile tests are shown in Figure 3.6, and the true stress-strain curves are shown in Figure 3.7. The result demonstrated that three curves as different directions with respect to the rolling direction were almost the same, representing a rather weak anisotropic behavior for heat treated SUS304 sheets. Thus, the sheet orientation was out of consideration in the follow-up research.
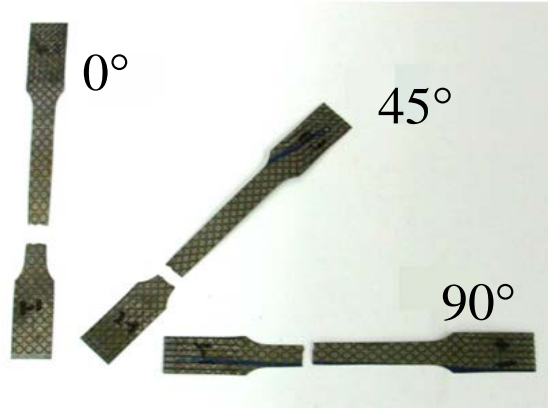
Figure 3.6: The heat treated specimens after the tensile tests.
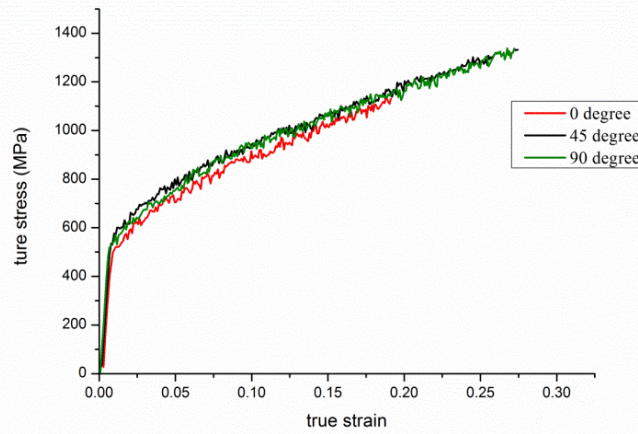
Figure 3.7: The uniaxial tensile test results for heat treated SUS304 specimens.

The true stress-true strain curves were fitted by the power law (see Eq. 6), and the rigid-plastic model is shown in Figure 3.8. The material properties of SUS304 sheets were obtained, and the corresponding parameters are presented in Table 3.1, Young's module of which is 195 GPa, and yield stress of which is 550 MPa.

$$\sigma_T = K(\varepsilon_T^p)^n + \sigma_y \qquad (6)$$

where ε_T^p is true plastic strain, σ_y is initial yield stress, E is Young's module, n is strain hardening exponent, and K is a constant.
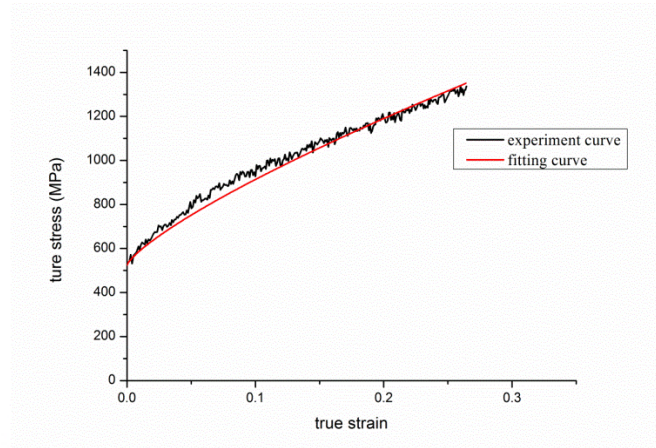
Figure 3.8: The fitting curve for heat treated SUS304 tensile test.

Table 3.1: The material properties of heat treated SUS304 sheets.

corresponding parameter	value
σ_y	550MPa
E	195GPa
n	0.92
K	2177.4

3.2 High-pressure hydroforming experiment

Hydroforming experiments were conducted using the apparatus to test its practicability, as well as to observe the formability of materials after high-pressure hydroforming. The hydroforming apparatus (see Figures 2.2 and 3.9) was set up with the following steps. First, the hydroforming apparatus provided the holding force to seal the working region, and the primary plunger in the hydroforming apparatus provided the pressure to induce the pressure fluid and to push the secondary plunger. Finally, the high-pressure fluid was generated in the high-pressure container to form the micro-flow channels. The pressure was released immediately after forming.

Figure 3.9: The hydroforming apparatus.

3.2.1 Formability experiment

A mold composed of SKD61 was developed, as shown in Figure 3.10a. The mold had an array of 26 parallel micro channels on an area of 40 mm × 40 mm. The selected micro channel sizes used in this study were 0.75 mm in channel width (W), height (H), and land area (S)(see Figure 3.10b) [17].
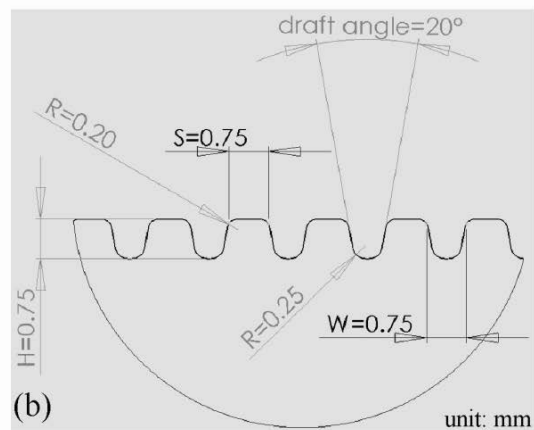
Figure 3.10: (a) A mold for hydroforming, and (b) geometries of micro-flow channels on the mold.

A series of experiments was conducted to assess the capability and repeatability of the hydroforming process for fabrication of metallic bipolar plates, with various hydrostatic pressures from 60 to 250 MPa applied to the specimens, and with a speed rate of 13 MPa min^{-1}. For each case, three replications were conducted to examine the repeatability of the process. To observe the formability of the hydroforming process, a laser sensor (Keyence LK-H020) with a high repeatability of 0.02 μm was used to measure the formed micro channel profiles (see Figure 3.11).
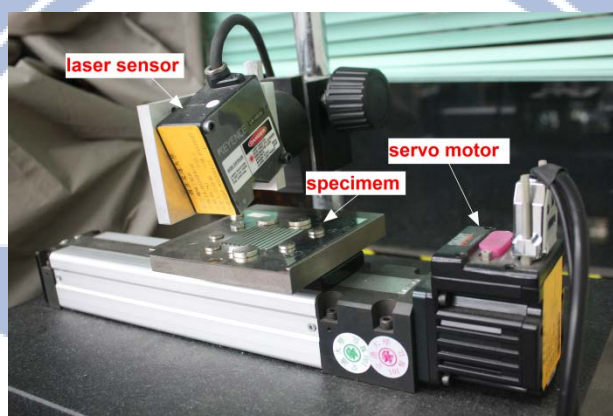
Figure 3.11: Laser measurement system (Keyence LK-H020 laser sensor).

Figure 3.12 shows that the pressure provided by the high-pressure apparatus in each test could reach the object pressure with a maximum forming pressure up to 250 MPa because of experimental safety. The method of fluid pressure measurement was attached in Appendix A. All the components in the apparatus worked smoothly; the high-pressure container sustained a pressure up to 250 MPa, and the high-pressure seal sealed the high-pressure fluid and maintained the high pressure. Finally, the feasibility of the high-pressure hydroforming technique, including a two-stage pressure increase structure, a high-pressure container, and a special seal, was verified.
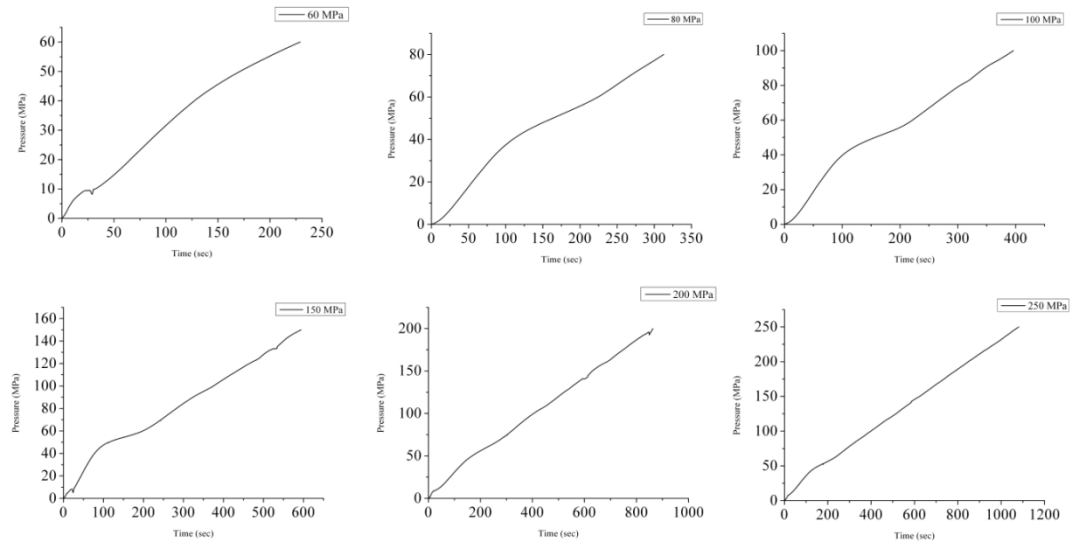
Figure 3.12: Pressure versus time for a series of hydroforming tests.

In addition, the maximum dimensional variation between various samples formed at the same pressure was approximately 7.48% (see Figure 3.13). Thus, this study reached the conclusion that the process control and repeatability of the micro-flow channel hydroforming were reasonably acceptable. The final detail specification of the high-pressure hydroforming apparatus are described in Table 3.2.
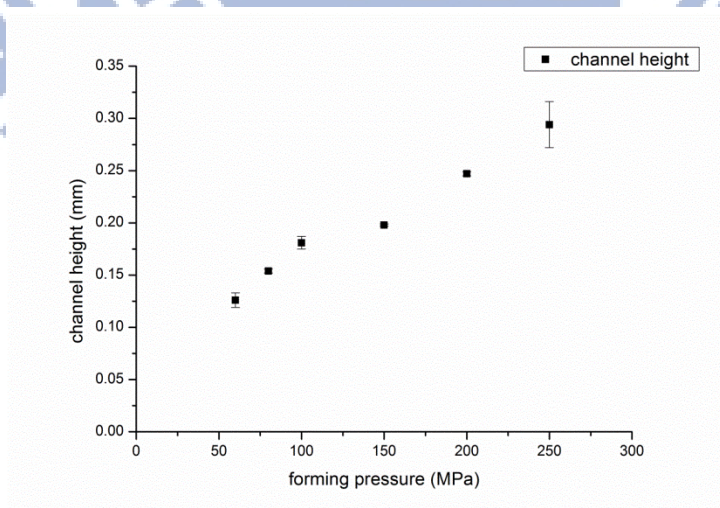
Figure 3.13: The dimensional variation between specimens in each test.

Table 3.2: The specification of the high-pressure hydroforming apparatus.

working temperature	room temperature
fluid pressure	40 – 250 MPa
pressure speed rate	13 – 26 MPa min^{-1}
holding force	0 –100 tons
working area	40 mm $\times$ 40 mm、Φ60 mm
sheet thickness	0.051– 1 mm
driving resource	servomotor
working voltage	220 V

Samples of the hydroformed bipolar plates are shown in Figure 3.14. The mold and typical profile measurements across the middle of the specimens and mold obtained from the laser sensor are shown in Figures 3.15 and 3.16. The measurements indicated that the dimension of the mold was approximately 0.76 mm and 0.75 mm in channel height and width, respectively, with a maximum in-plate height variation of 0.78% (see Figure 3.15). The dimension of the mold was similar to that of the mold design, which was 0.75 mm in channel height and width.
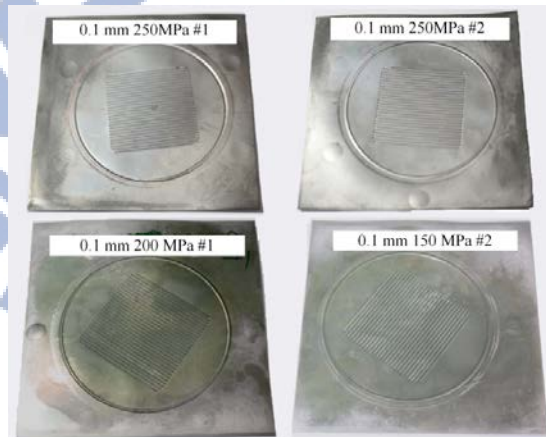
Figure 3.14: Samples of hydroformed specimens.
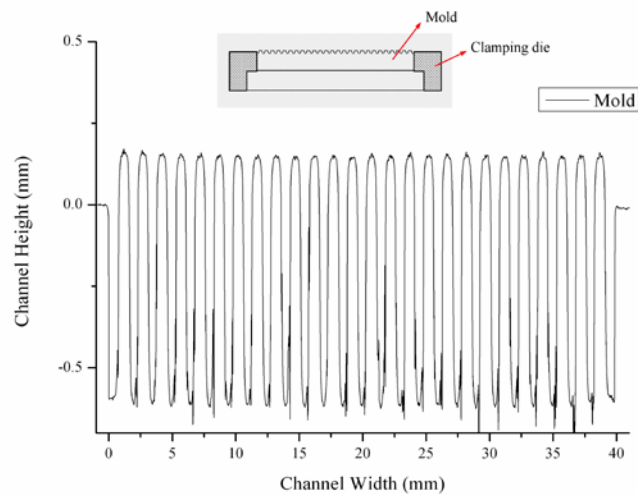
Figure 3.15: Laser measurement profiles for the mold.

However, the profiles of specimens shown in Figure 3.16 had a concave shape, in which the channels on both sides were bulging. This occurred because the specimens were not flat, especially after the solution heat treatment; nevertheless, the channel heights on both sides did not differ from other channel heights on the specimen. The formability among micro-flow channels within the same bipolar plate was uniform with a maximum in-plate height variation of 2.5%.
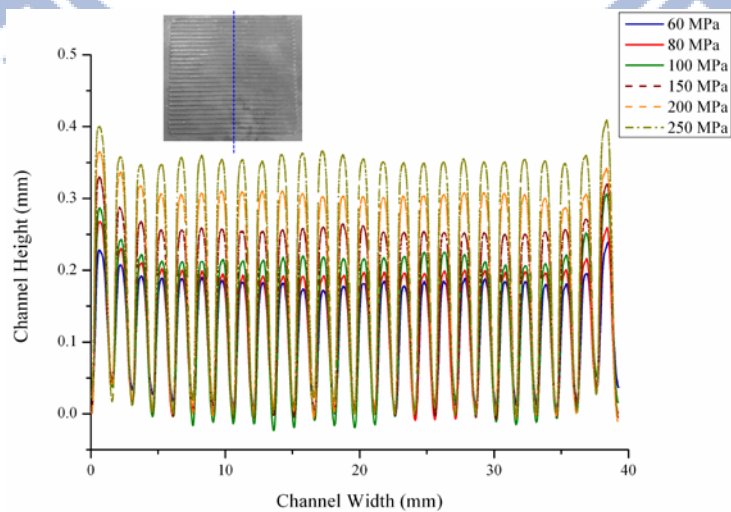
Figure 3.16: Laser measurement profiles for hydroformed specimens.

In previous studies [1, 17-18], traditional hydroforming process had been limited by the forming pressure, and formed micro-flow channels on 0.051-mm-thick SUS304 plates with a maximum aspect ratio of 0.31, which prevented the cell performance from being revealed effectively. In our preliminary tests, heat treated SUS304 specimens with 0.051 mm thickness was tested by the developed apparatus, and the result (see Table 3.3) confirmed that formed channel aspect ratio on heat treated SUS304 blanks reached 0.39 with increasing working pressure up to 150 MPa, which could verify that high-pressure hydroforming technique is indeed helpful for promoting the formability of specimens. However, to meet the requirement on the strength of practical bipolar plates, heat treated SUS304 specimens with 0.1 mm thickness were selected in the follow-up research.

Table 3.3: A comparison of experiment results in our research and the related literature.

	sheet thickness	pressure	aspect ratio
Mahabunphachai,[17]	0.051 mm	60 MPa	0.310
	0.051 mm	150 MPa	0.390
this research	0.1 mm	60 MPa	0.168
		80 MPa	0.205
		100 MPa	0.241
		150 MPa	0.264
		200 MPa	0.329
		250 MPa	0.392

From the experiment results (see Table 3.3), the aspect ratio of the micro-flow channels formed on the 0.1-mm-thick SUS304 plates reached 0.392 at 250 MPa working pressures by using the proposed high-pressure hydroforming technique, the result of which revealed that, compared with the channel aspect ratio of 0.31 formed

by tradition hydroforming technique, an aspect ratio of formed micro channels could be promoted up to 26.5%. Hence, the high aspect ratio micro-flow channel on a reinforced metallic plate may be obtained using this high-pressure hydroforming apparatus to meet both cell performance and manufacturing requirements.

3.2.2 Forming uniformity experiment

To comprehensively observe the uniformity effect for this high-pressure hydroforming process, the uniformity of micro flow channels on the formed specimen with 250 MPa working pressures was observed. The laser sensor was utilized to measure the uniformity of the micro channels at three different locations, i.e. the left, middle, and right of micro channels. Figure 3.17 shows that, at 250 MPa working pressures, in-plate height variations of three different locations (the left, middle, and right of micro channels) in three replications were 2.4%, 3.5%, and 1.8%, respectively. Besides, the average channel heights in each location were 0.292, 0.287, 0.284 mm, the deviation of which was approximately 2.7%. Thus, from these experiment results, the micro channels formed by this developed high-pressure hydroforming technique had great uniformity.
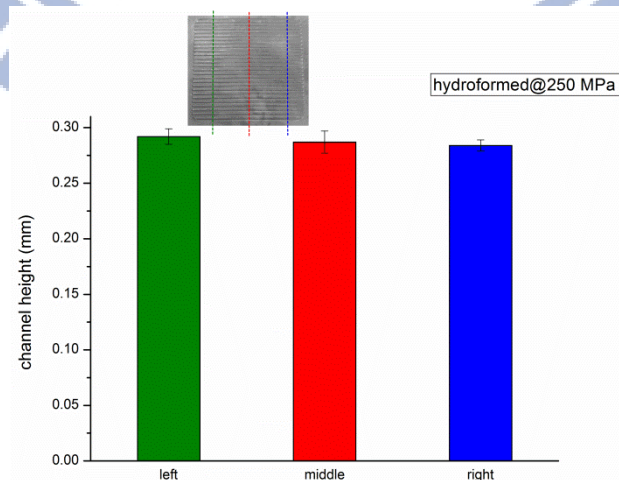
Figure 3.17: Height variations in three different locations of micro channels.

Furthermore, the working area was located at the center of a SUS304 blank with an area of 40 mm $\times$ 40 mm, and the working area subsequently needed to be cut and installed in fuel cells. Thus, in this research, the working area was cut using wire cut to observe its deformation condition. Figure 3.18a shows that, before cutting working area, there was tilting around the specimen with a dimension of 100 mm $\times$ 100 mm, and Figure 3.18b shows, after cutting, although there was still a little tilting around the working area with a dimension of 40 mm $\times$ 40 mm, deformation of working area was great uniformity, and no distortion occurred on working area.
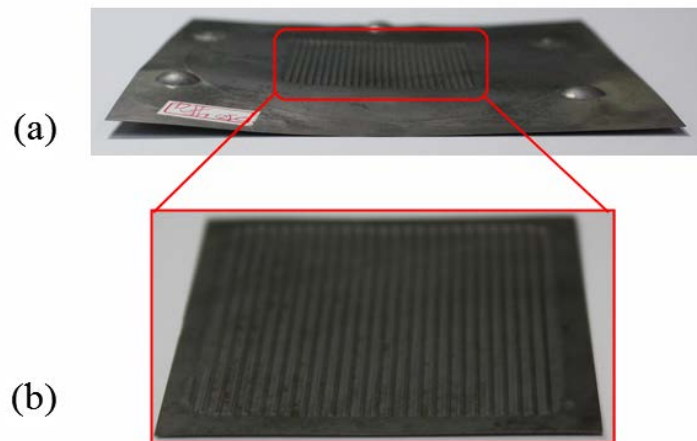
Figure 3.18: Side views of (a) the specimen and (b) the working area.

Finally, micro channels on the hydroformed specimens with the working pressure from 60 to 250 MPa were cut across the middle of the micro channels using wire cut, and a microscope with a magnification factor of 19.7 was used to further observe the variation of sheet thickness. Figures 3.19 show that, under various pressures from 60 to 250 MPa, thickness variations of specimens were quite uniform with a maximum reduction ratio of 13.2% (see Table 3.4) and no obviously local attenuation. The result confirmed the uniformity effect of this developed technique. Beyond that, Figures 3.19 demonstrated that the shape of micro channels was

obviously hydroformed with increasing working pressure up to 100 MPa, which verified that the development on the high-pressure hydroforming technique was necessary.
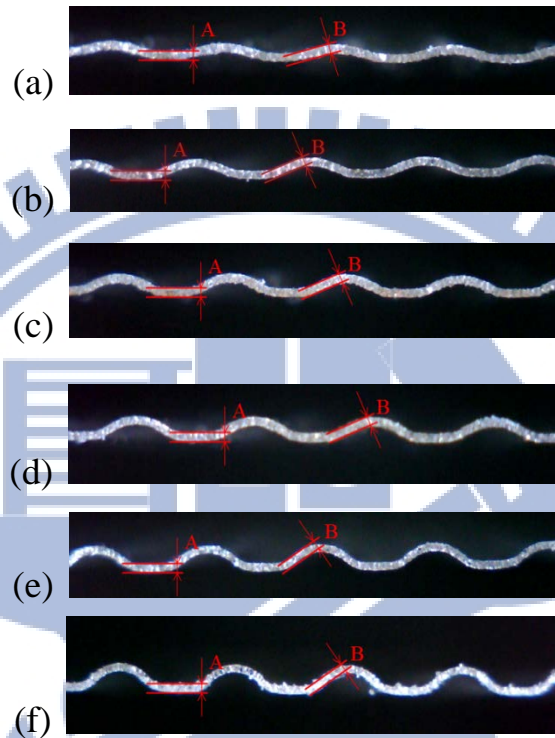
Figure 3.19: Thickness variation of specimens at (a) 60 MPa,(b) 80 MPa,(c) 100 MPa,(d) 150 MPa,(e) 200 MPa, and (f) 250 MPa.

Table 3.4: The reduction ratio of each specimen thickness.

	thickness variation		
pressure	location A	location B	reduction ratio ($\frac{A-B}{A} \times 100\%$)
60 MPa		0.118 mm	2.42%
80 MPa		0.117 mm	3.20%
100 MPa	0.121 mm	0.115 mm	4.96%
150 MPa		0.115 mm	4.96%
200 MPa		0.108 mm	10.70%
250 MPa		0.105 mm	13.20%

3.2.3 Forming parameters experiment

From previous literatures [1, 18], the geometries of micro channels could affect the formability of the specimen. To be helpful for a design variable selection in the follow-up optimization analysis, a series of forming parameters experiments were conducted first, and a mold composed of SKD61 was constructed, as shown in Figure 3.20 and Table 3.5. The mold had an array of 13 parallel micro channels on an area of 40 mm × 40 mm. The selected micro channel sizes used in this study were 0.5, 0.75,1 and 1.5 mm in channel width, and each channel width had three or four channels to conveniently observe the formability at the same width. Then, land area, channel height, and draft angle were a constant of 1.5 mm, 0.5 mm, and 20°, respectively, to neglect their effects on formability, and the working pressures of 150 MPa and 250 MPa were selected.
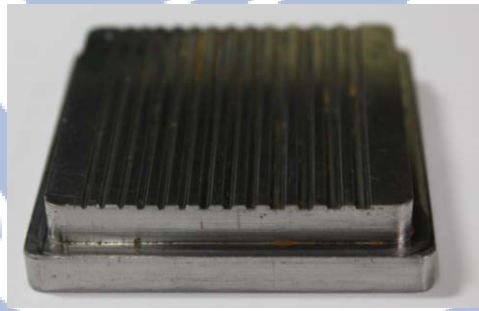
Figure 3.20: A mold of the forming parameters experiment.

Table 3.5: Detail geometry of micro-channels for the forming parameters experiments.

feature	group I	group II	group III	group IV
no. of channels	3	3	3	4
channel width W	0.5	0.75	1	1.5
channel height H		0.5		
draft angle α		20°		
land area S		1.5		

dimension of micro channels (unit: mm)

*Land area means the distance between channels
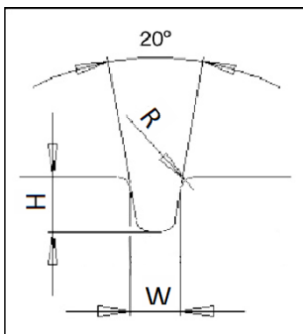
The experiment result (see Table 3.6 and Figure 3.21) demonstrated that, on the effect of channel widths on the mold, when channel widths increased 3 times, from 0.5 mm to 1.5 mm, the formed channel aspect ratio between group I and group IV was promoted by 26.70% at 150 MPa, and the formed channel aspect ratio was improved by 27.81% at 250 MPa. On the other hand, on the effect of forming pressure, when forming pressure increased 1.67 times, from 150 to 250 MPa, the formed aspect ratio was promoted by 15.60%, 5.51%, 5.14%, and 16.89% at group I, II, III, IV respectively. The great improvement of formed channel aspect ratio occurred at group I and group IV because those channels were located on the edges of the mold and were less limit on material flow at higher fluid pressure.

To further observe the effects between the channel width on the mold and forming pressure, the results of group II and group III were observed, the channel width on the mold of which increased 1.33 times. The formed channel aspect ratio was promoted by 7.08% at 150 MPa, and the formed channel aspect ratio was improved by 6.72% at 250 MPa. From these results, channel width on a mold and forming pressure could obviously affect the formed channel aspect ratio on specimens, and the effect of channel widths on the mold with the improvement of formed channel aspect of 6.72% and 7.08% was greater than that in forming pressure with the improvement of 5.14% and 5.51%.

Table 3.6: A comparison of experiment results at 150 and 250 MPa.

hydroformed channel aspect ratio

| | group I | group II | group III | group IV |
channel width on a mold	0.5 mm	0.75 mm	1 mm	1.5 mm
150 MPa	0.184	0.223	0.240	0.251
250 MPa	0.218	0.236	0.253	0.302
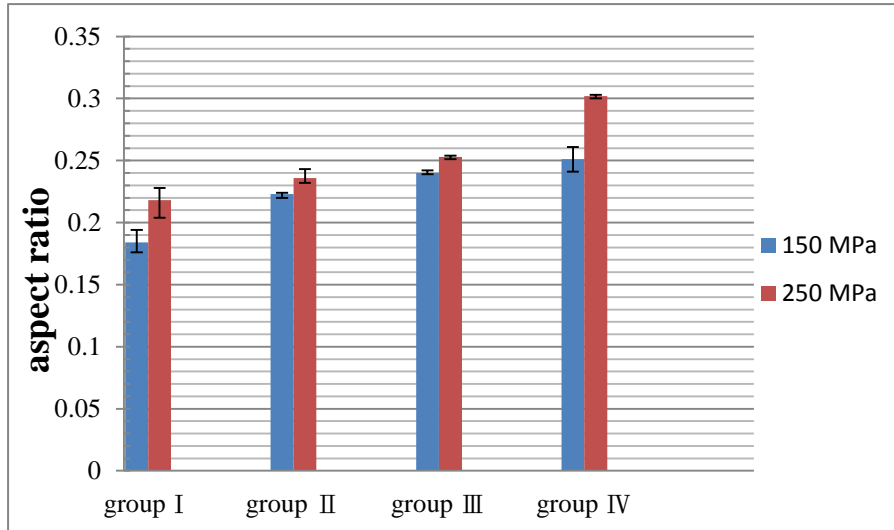
Figure 3.21: A comparison of experiment results at 150 and 250 MPa.

3.3 Preliminary fuel cell performance test

To further make sure the feasibility of hydroformed specimens applied in fuel cells, two pairs of metallic bipolar plates were performed using working pressure of 150 MPa and 250 MPa respectively, and then a fuel cell with a pair of metallic bipolar plate was assembled to test its preliminary cell performance. The flow field design referred to that in Liu's research [15-16], and the selected micro channel sizes were 1.2, 0.5, and 1.0 mm in channel width, channel height, and land area, respectively, as shown in Figure 3.22 and Table 3.7. Measuring equipment, TEI-P300-1AB2CS, was utilized, and the cell specifications are shown in Table 3.8. The cell was fabricated with an end plate, gasket, bipolar plate, gasket, electrode, and proton exchange membrane in turn, as shown in Figure 3.23.
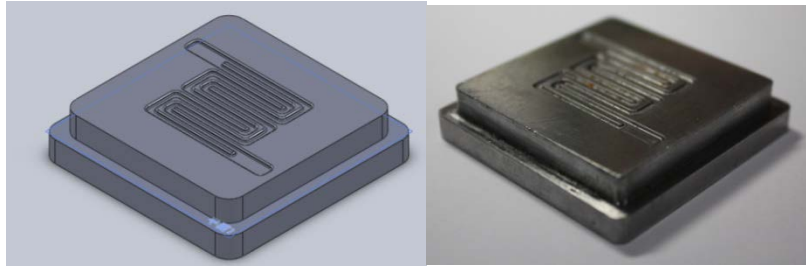
Figure 3.22: A mold for the flow field.

Table 3.7: The dimension of the flow field.

dimension of micro channels (unit: mm)	
channel width W	1.2
channel height H	0.5
chamfering angle R	0.2
land area S	1.0

Table 3.8: Cell specifications.

part	specification
proton exchange membrane	DuPont NRE212 Dimension: $30 \times 30 \times 0.05$ mm
GDE	CARBEL®CL Pt 0.35 mg cm^{-2} Dimension: $23 \times 23 \times 0.3$ mm
metallic bipolar plate	Stainless steel SUS304 Dimension: $40 \times 40 \times 0.1$ mm
end plate	PMMA Dimension: $55 \times 55 \times 10$ mm
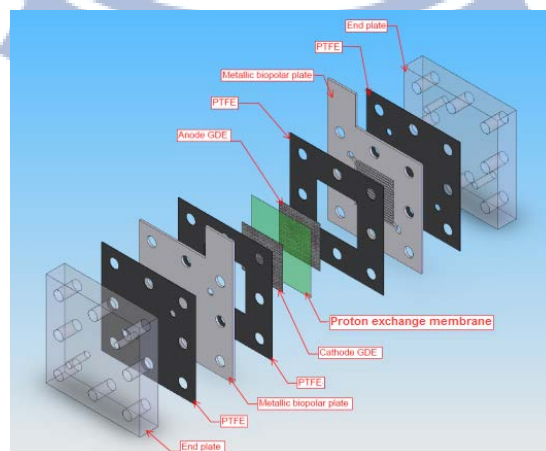
Figure 3.23: Schematic representation of metallic bipolar plate fuel cell assembling.

In fuel cell performance test, a single cell (see Figure 3.24) was assembled with the dimension of $50 \times 50 \times 23$ mm including a pair of metallic bipolar plates (see Figure 3.25), the electrodes and the proton exchange membrane (see Figure 3.26) and then was tightened by 15 Kg cm^{-2} torque. Leak indicator fluid was daubed around the cell, and hydrogen and oxygen were the fuels for the anode and cathode electrodes, respectively, the flow rate of which was 60 c.c. min^{-1} at room temperature having air admission pressure of an atmospheric pressure.

Figure 3.24: A single fuel cell assembly.
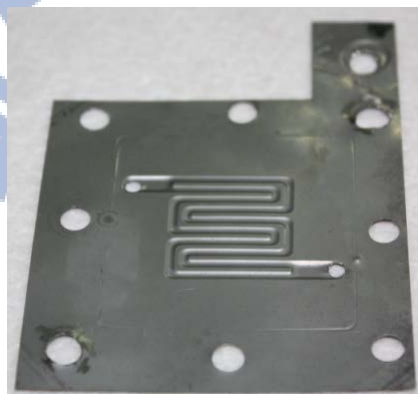
Figure 3.25: A hydroformed metallic bipolar plate.
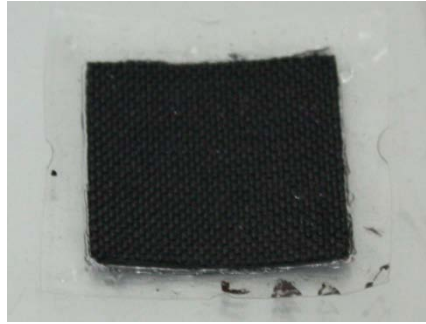
Figure 3.26: The electrodes and proton exchange membrane.

Figure 3.27 shows a comparison of fuel cell performances with hydroformed metallic plates using forming pressure of 150 and 250 MPa respectively. A single cell with metallic bipolar plates formed by 150 MPa working pressures (an aspect ratio of 0.18) had the maximum power density of 310.57 mW cm^{-2}, and the maximum power density in a cell using metallic bipolar plates formed by 250 MPa working pressures (an aspect ratio of 0.25) reached 360.82 mW cm^{-2}. This result confirmed not only the feasibility of hydroformed metallic bipolar plates but also the improvement of the cell performance with increasing channel aspect ratio on bipolar plates. Furthermore, the reason for the influence between channel aspect ratio and cell performance was proposed in Hung's research [13], where the electrodes and proton exchanges membrane were deformed and pushed into the channel when cell fabricating resulting in decreasing the cross-section area of the flow channel; therefore, reaction gas flowing and water draining were impeded causing low cell performance.

However, the improvement of the cell performance between 150 and 250 MPa shown in Figure 3.27 was not obvious with an increase in channel aspect ratio. The reason was that the water generated when cells were working was piled up in the flow field of this test and made the reduction of the cell performance. In addition, the geometries of micro channels used in this test were not suitable for hydroforming; therefore, finite element and optimization analyses were conducted to efficiently

promote the channel aspect ratio on specimens using high-pressure hydroforming technique in the follow-up research.
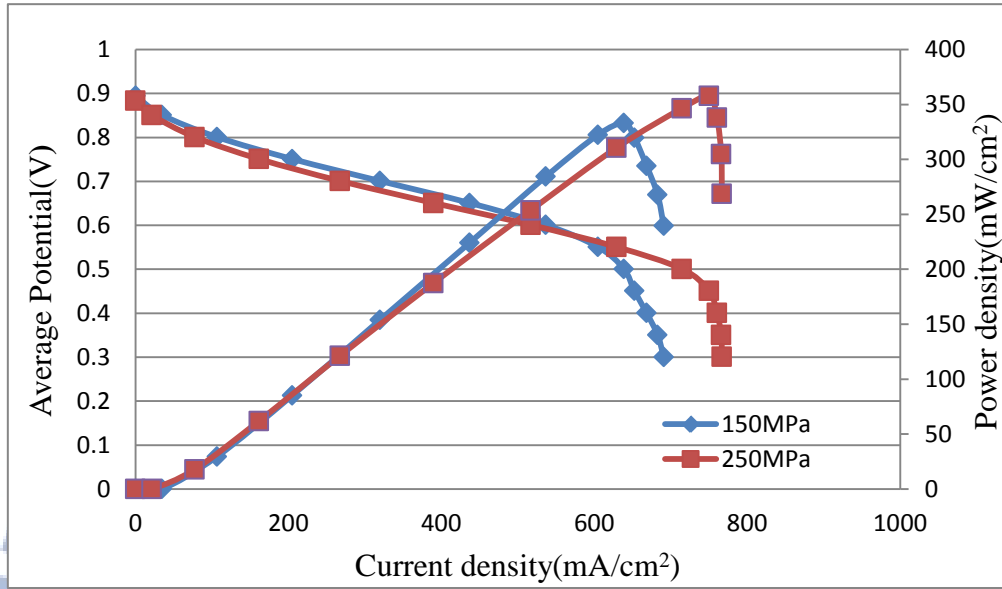
Figure 3.27: A comparison of fuel cell performances.
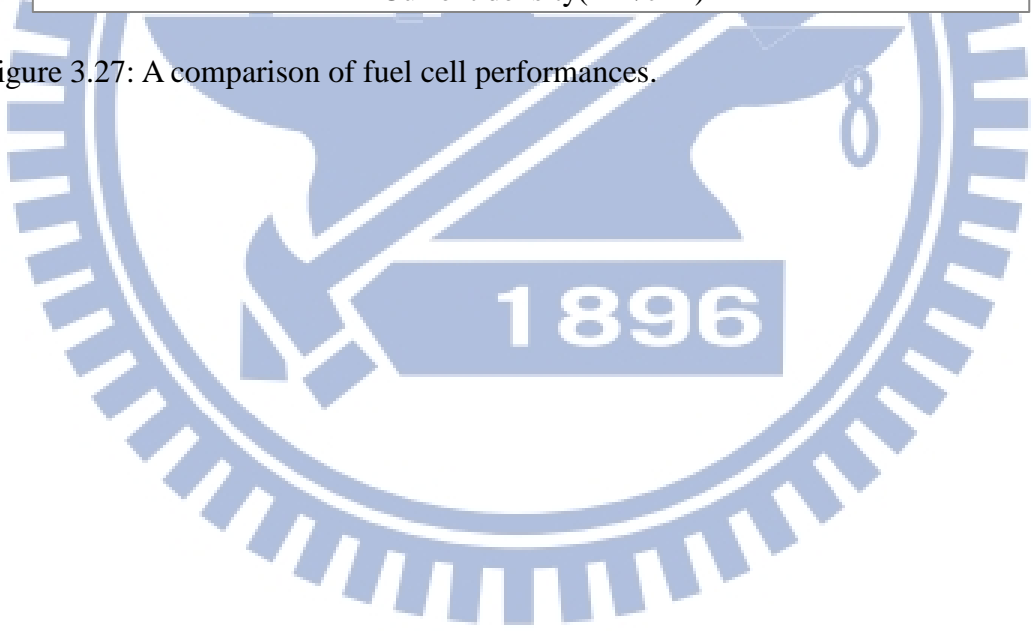
CHAPTER 4 NUMERICAL INVESTIGATIONS OF THE
HIGH-PRESSURE HYDROFORMING TECHNIQUE

To reveal the full capability of this developed apparatus, finite element analysis software was used to analyze the hydroforming process, and the optimization software subsequently predicted the possibly optimal aspect ratio of micro-flow channels using the verified finite element model. In the end, the verification experiment of the optimization analysis was conducted to confirm the precision of the optimization analysis. Thus, a complete high-pressure hydroforming technique was developed.

4.1 Finite element analysis

The material properties obtained by a tensile test were imported to Abaqus/Standard to analyze the hydroforming process (see Figure 4.1). A computer with Intel Core i5-3450 CPU @ 3.10GHz 3.50 GHz, 8GB ram, and Win 7 professional-64 bit was utilized. The assumptions of the finite element analysis in this research were as follows: 1) the deformation of the specimen was plane strain, and the properties of the specimen were homogeneous, isotropic, and elasto-plastic; 2) the mold was defined as a rigid body; 3) the fluid pressure was uniformly worked on the specimens; and 4) the changes of the pressure from the leakage of the high-pressure fluid were neglected.
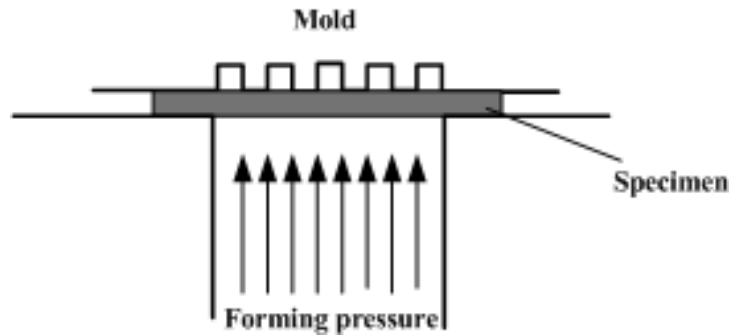
Figure 4.1: Schematic of the position of molds and specimen.

The 2-D simulation model having 26 micro channels was constructed (see Figure 4.2) according to the mold and specimen of the formability experiment. Solid elements (CPE4R) were used. To consider the precision and efficiency of the simulation, the convergence test for the mesh sizes was conducted with the working pressure of 100 MPa, the mesh sizes of which were set as 0.034, 0.025, and 0.02 mm, and the influence between mesh size and formability was investigated. Figure 4.3 shows that the variation of the channel height between mesh sizes of 0.034 and 0.025 mm was approximately 1.68%; however, the variation between mesh sizes of 0.025 and 0.02 mm was approximately 0.12%. The formability of the simulation was tending to relatively stable at mesh size of 0.025 mm with reducing mesh size. Thus, the mesh size of 0.025 mm was adopted to be used in the follow-up research.
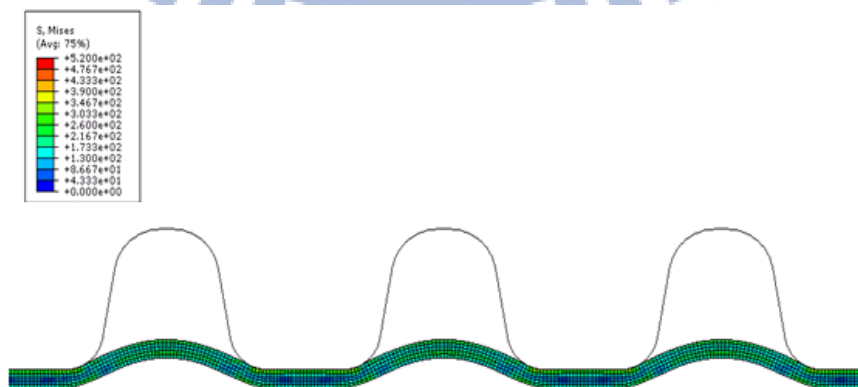
Figure 4.2: The 2-D high-pressure hydroforming simulation model.
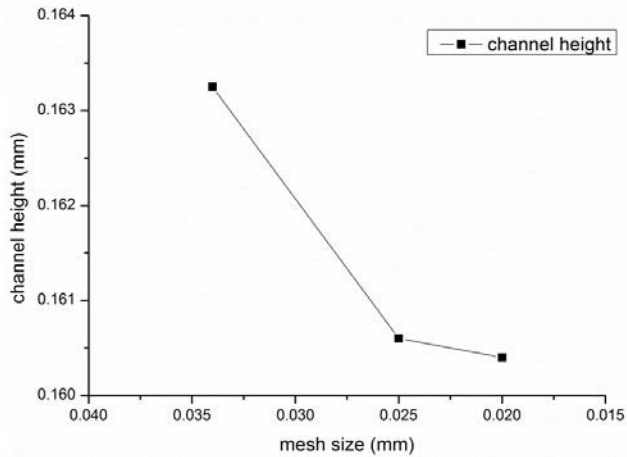
Figure 4.3: The relationship of mesh sizes and formed channel height.

For boundary conditions, the coefficient of friction between the mold and specimen was set to 0.1 [39]. The freedom of in-plate direction on both sides of the specimen was fixed according to the practical design of the apparatus; the uniform pressure from 60 to 250 MPa was exerted on the specimen and subsequently released. Finally, the precision of the finite element model was verified by comparing simulations with experiments.

Figure 4.4 shows that the tendency of the simulation result for the complete model having 26 micro channels was similar to that in formability experiments with a maximum deviation of 10.37%, verifying the precision of the finite element model. However, the finite element model can be simplified to allow smooth optimization analysis and observation. The micro channels on the center of working area were selected to observe their formability, and the results among the simplified model, the complete model, and hydroforming tests were compared to ensure the precision of the simplified model. The results indicated that no substantial differences occurred among the results (see Figure 4.4). Therefore, the follow-up optimization analysis was conducted using this verified simplified finite element model.
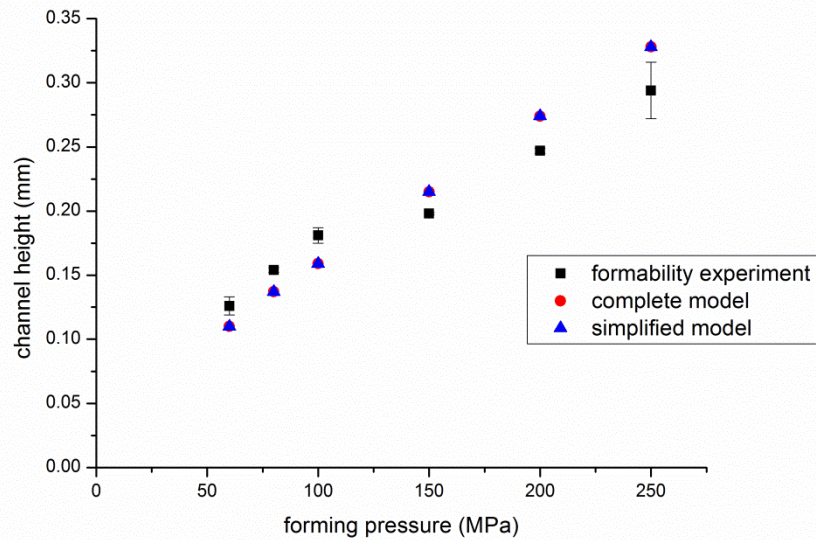
Figure 4.4: A comparison of the simplified model, the complete model, and hydroforming tests.

Besides, the simulation result found that the maximum equivalent strain on the specimen was 0.43 located on the chamfering angle of opening of micro-flow channels when working pressure reached 250 MPa (see Figure 4.5), which was selected as a constraint in the follow-up optimization analysis. This simulation result also confirmed the results of previous forming uniformity experiments that thickness variations of specimens were quite uniform and maximum reduction ratio occurred on the chamfering angle of opening of micro-flow channels. Figure 4.6 shows the displacement of the specimen, and the land area on the specimen was fixed by high fluid pressure, which limited material movement flowing into channels on the mold. Figure 4.7 shows the distribution of von Mises stress on the specimen, and the chamfering angle of opening of micro-flow channels on the specimen suffered bending force, which also limited material movement flowing into channels. Besides, the bottom of channels on the specimen suffered tension force pulling the material.

Finally, attenuation occurred on the chamfering angle of opening of micro-flow channels.
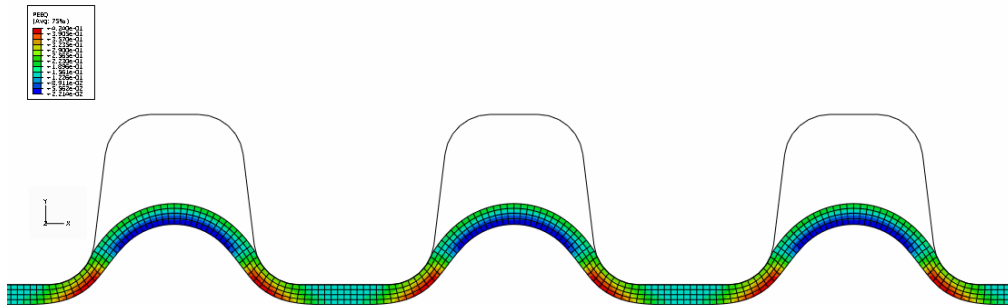
Figure 4.5: The equivalent strain contour on the specimen at 250 MPa.
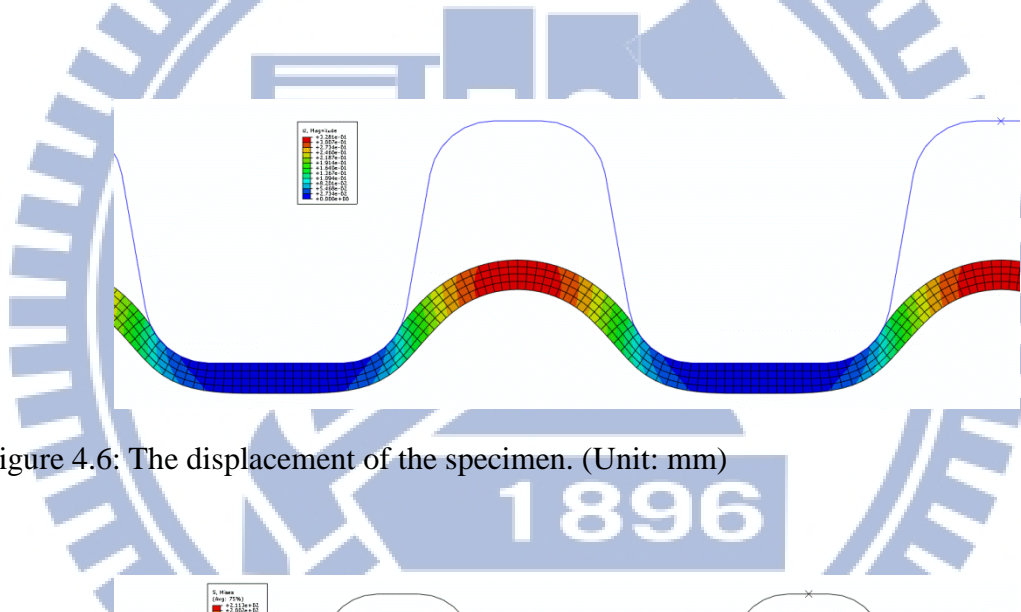
Figure 4.6: The displacement of the specimen. (Unit: mm)
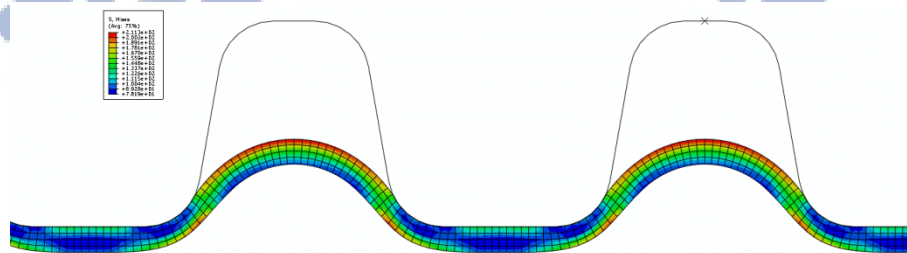
Figure 4.7: The distribution of von Mises stress on the specimen. (Unit: MPa)

4.2 Optimization analysis

SmartDO is a multidisciplinary design optimization software based on the Direct Global Search technology developed and marketed by FEA-Opt Technology.

SmartDO specialized in the CAE-Based optimization, such as CAE (computer-aided engineering), FEA (finite element analysis), CAD (computer-aided design), CFD (Computational fluid dynamics) andautomatic control, with application on various physics phenomena. It is both GUI and scripting driven, allowed to be integrated with almost any kind of CAD/CAE and in-house codes. SmartDO focuses on the direct global optimization solver, which does not need much parametric study and tweaking on the solver parameter. Because of this, SmartDO has been frequently customized as the push-button expert system [40].

To fully reveal the capability of the experimental apparatus, the optimization analysis was conducted in this research by modifying the dimension of micro-flow channels on the mold to form the extreme high-aspect-ratio micro-flow channels.

SmartDO was connected to the finite element software, and the aspect ratio of the micro-flow channels on formed specimens was chosen as the object function. In preliminary formability tests, the working pressure of 250 MPa was successfully exerted on the specimens. Simultaneously, the finite element analysis for 250 MPa working pressures exerted on the specimens was conducted, and the result indicated that the maximum equivalent strain on the specimen was 0.43 located on the chamfering angle of the opening of micro channels. To avoid the rupture of the specimen, the equivalent strain of the specimen was set to equal or below 0.43 as the constraint. According to the related literature [39] and our practical experience, the selection and the ranges of design variables were a channel width of 0.5–1.5 mm, a land area of 0.5–1.5 mm, and a draft angle of $14-20°$, as shown in Table 4.1.

Table 4.1: The selections and the ranges of design variables.

design variables	range
channel width W	0.5 –1.5 mm
land area S	0.5 –1.5 mm
draft angle α	$14-20°$

Figure 4.8 shows the convergence curve for the optimization analysis, and Table 4.2 shows a comparison among the results of the formability experiments, the optimization analysis, and Mahabunphachai's research [17]. A group of possibly optimal forming parameters obtained by the optimization analysis was 0.803 mm, 1.5 mm, and 14° in channel width, land area, and draft angle respectively, and 250 MPa working pressures was offered. The predicted channel height might reach 0.415 mm with an aspect ratio of 0.517, which was greater than the aspect ratio of 0.31 formed by Mahabunphachai's research [17] and the aspect ratio of 0.392 obtained by the formability experiments of this research. Besides, the equivalent strain of the formed specimen and the profile of the mold obtained by the optimization analysis are shown in Figure 4.9. The maximum equivalent stain was 0.43, which was within the constraint (the equivalent stain ≤ 0.43).
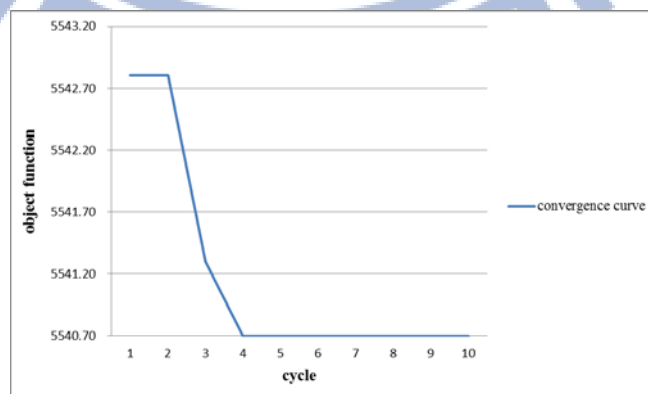
Figure 4.8: Convergence curve for the optimization analysis.

Table 4.2: A comparison of hydroforming tests, optimization analysis, and literature.

	micro-flow channels on the mold			forming pressure	sheet thickness	aspect ratio
	width W	land area S	draft angle α			
Mahabunphachai, [17]	0.75 mm	0.75 mm	20 °	60 MPa	0.05 mm	0.310
formability experiment	0.75 mm	0.75 mm	20 °	250 MPa	0.10 mm	0.392
2D optimization prediction	0.803 mm	1.5 mm	14 °	250 MPa	0.10 mm	0.517
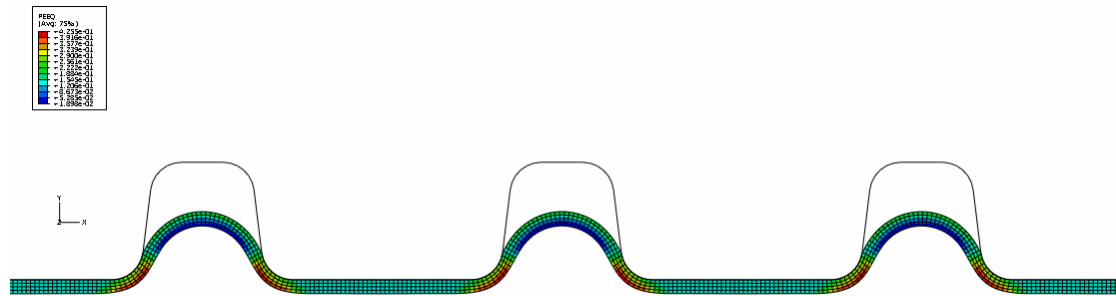
Figure 4.9: The equivalent strain of the formed specimen and the profile of the mold.

4.2.1 The verification experiment of the optimization analysis

The verification experiment for a group of forming parameters was conducted according to the optimization analysis, and a mold composed of SKD61 was constructed. The mold had an array of 15 parallel micro channels, and the selected micro channel sizes used in this study were 0.80 mm, 1.5 mm, and 14° in channel width, land area, and draft angle respectively (see Figure 4.10). The working pressure was set as 250 MPa.

Figure 4.10: A mold of the verification experiment.

A sample after the verification experiment is shown in Figure 4.11. After measuring specimens by the laser sensor, channel heights were approximately 0.33 mm with an aspect ratio of 0.411. Although the aspect ratio (0.411) in the verification experiment was greater than an aspect ratio of 0.392 in previous formability experiment, the deviation between 2D optimization prediction (0.517) and the verification experiment result (0.411) was up to 20.5%. The deviation occurred because of the much simplified boundary condition in 2D simulation. To solve this issue and obtain precise analyses, 3D simulation model was necessary to be constructed according the practical high-pressure hydroforming process, and then the optimization analysis was re-conducted using the verified 3D simulation model.
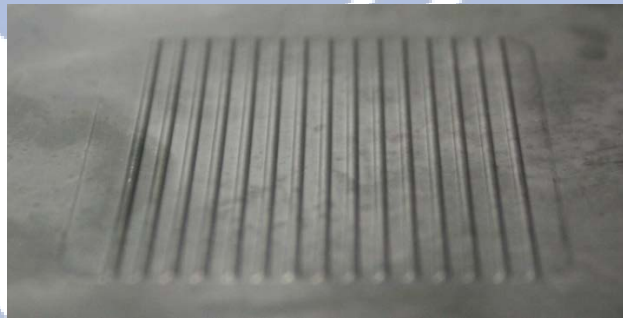
Figure 4.11: A sample after the verification experiment.

4.2.2 3D finite element analysis

3D high-pressure hydroforming model was constructed using Abaqus/Explicit, which is suitable for solving thin metal blanks forming, fracture, and no-linear problems. A quarter symmetry model having an array of 13 parallel micro channels and a working area of $20 \times 20 \, \text{mm}^2$ on a mold was constructed according to the formability experiment (see Figure 3.10), and the mold was defined as a rigid body. The material properties of SUS304 blanks were homogeneous, isotropic, and

elasto-plastic, and shell elements (S4R) were used. After the convergence test, the mesh size of 0.1 mm was selected.

For boundary conditions, the coefficient of friction between the mold and specimen was set to 0.1 [39]. The edges of the specimen were fixed according to the practical design of the apparatus; various pressures from 60 to 250 MPa was exerted on the specimen and subsequently released.

The simulation result (see Figure 4.12) shows that, at 250 MPa working pressure, the channel height could reach 0.309 mm with an aspect ratio of 0.412. Compared with the formability experiment result (an aspect ratio of 0.392), the deviation was approximately 4.85%, verifying the precision of the simulation model. However, a computational task of a quarter symmetry model was extremely heavy, spending more than 9 hours. Thus, 3D simplified model having three channels with a length of 10 mm was constructed. The result (see Figure 4.13) found that the channel height reached 0.307 mm with an aspect ratio of 0.408, which was similar to the result of a quarter symmetry model with the deviation of 0.97%, and the computational time was only one hour. Moreover, Figure 4.14 shows a comparison of pervious formability experiment results and 3D simplified simulation results and confirms the precision of 3D simplified model.
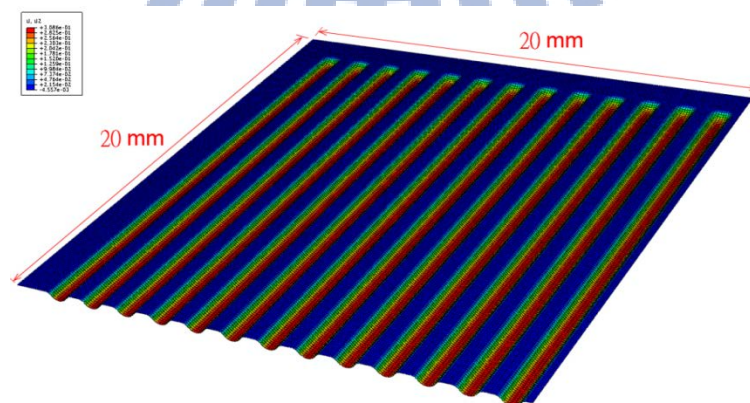
Figure 4.12: The channel height for a quarter symmetry model. (Unit: mm)
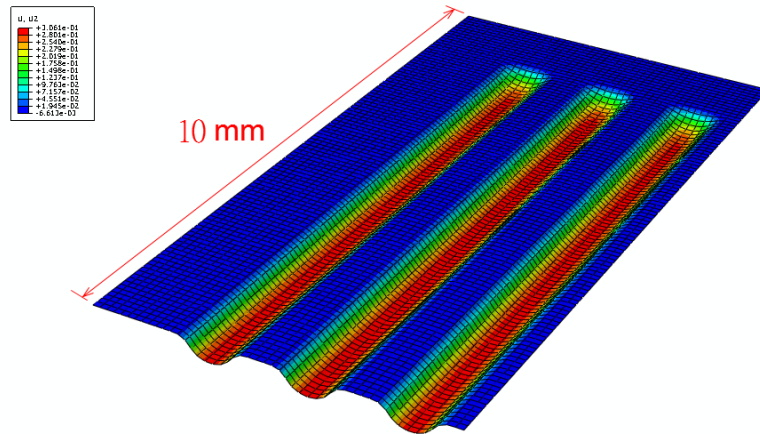
Figure 4.13: The channel height for a 3D simplified model. (Unit: mm)
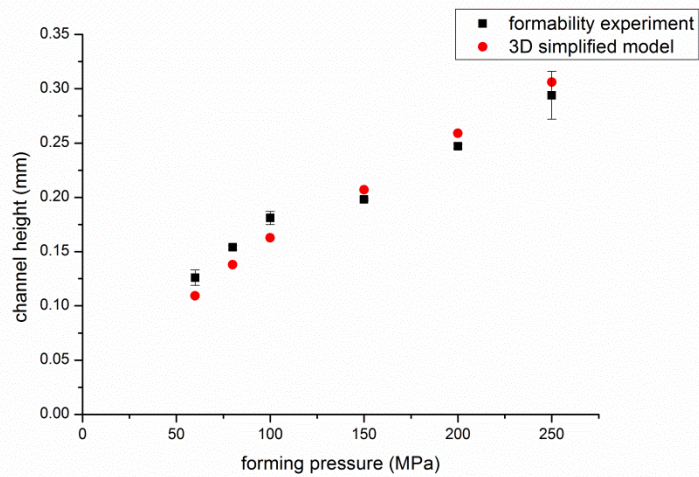
Figure 4.14: A comparison of 3D simplified model simulations and formability experiments.

4.2.3 3D optimization analysis

Optimization analysis was conducted using the verified 3D simplified model, and the object function, constraint, and design variables were the same as the previous research. A group of optimal forming parameters was found (see Table 4.3), which was similar to that in 2D optimization prediction. The variation between 2D and 3D

optimization predictions was only 0.006 mm in channel width, which was smaller than the machining accuracy of traditional fabricating methods; therefore, there was no need to conduct verification experiments for 3D optimization prediction. In 3D optimization prediction, the predicted channel height reached 0.362 mm with an aspect ratio of 0.452 and maximum equivalent strain on the specimen still occurred on the chamfering angle of opening of micro-flow channels, as shown in Figures 4.15 and 4.16. Compared between 3D optimization prediction and the verification experiment, the deviation reduced to approximately 10%, which was better than that in 2D optimization prediction. Hence, a precise optimization analysis was developed. From the optimization analysis, a formed channel aspect ratio could be promoted by 4.8% from 0.392 in formability experiments to 0.411, which could efficiently reveal the forming capability of the developed technique.

In addition, from the comparisons between 2D and 3D optimization predictions, 2D finite element and optimization analyses was found to be efficient because of shorter spending time, simpler analyses, and acceptable optimal forming parameters (see Table 4.3 and Table 4.4).

Table 4.3: A comparison of verification experiments and optimization predictions.

| | micro-flow channels on the mold | | | forming pressure | channel height | aspect ratio |
	width W	land area S	draft angle α			
2D optimization prediction	0.803 mm	1.5 mm	14 °	250 MPa	0.415 mm	0.517
3D optimization prediction	0.809 mm	1.5 mm	14 °	250 MPa	0.362 mm	0.452
verification experiment	0.800 mm	1.5 mm	14 °	250 MPa	0.330 mm	0.411
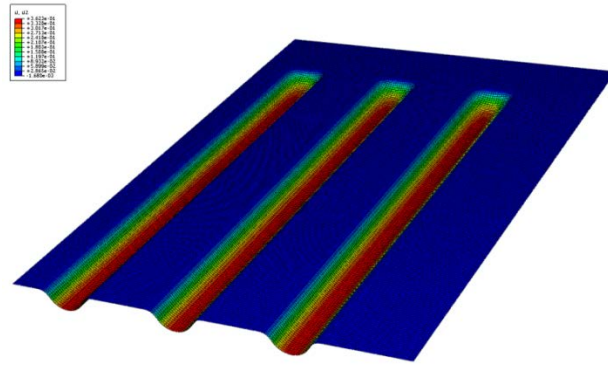
Figure 4.15: The channel height for 3D optimization model. (Unit: mm)
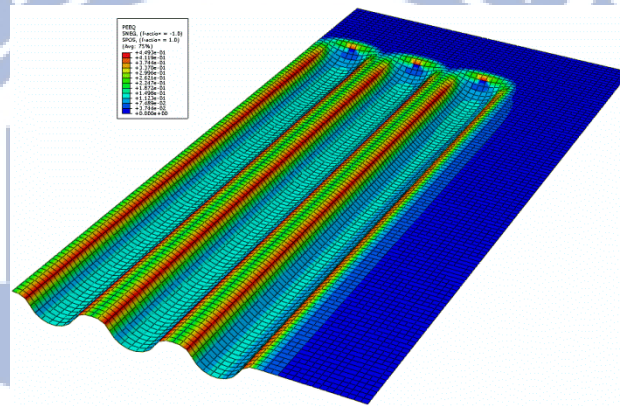
Figure 4.16: The distribution of equivalent strain for 3D optimization model.

Table 4.4: A comparison of 2D and 3D simplified finite element model

	element numbers	FEM operation time	optimization analysis operation time
2D simplified model	1200	0.25 hr	1 hr
3D simplified model	6900	1 hr	72 hr

4.2.4 A flow field design on the metallic bipolar plate

In this study, the aspect ratio of micro channels on bipolar plates was investigated to promote the fuel cell performances; however, in practical fuel cells, not only the channel aspect ratio but also an opening ratio ($W_1+W_2+\ldots/ L$) (see Figure 4.17) on bipolar plates can affect the fuel cell performances. To act as a reference for follow-up flow field designs on metallic bipolar plates, an opening ratio was added as

54

a constraint using the verified optimization analysis. In the flow field design, an opening ratio on the metallic bipolar plates has an optimal value of approximately 45–75%. The contact resistance between electrodes and bipolar plates is extremely higher when the opening ratio is higher, which reduces the fuel cell performance. By contrast, available efficiency of the electrodes is extremely lower when the opening ratio is lower, which also reduces the fuel cell performance and increases the resistance of reactive gas [42].
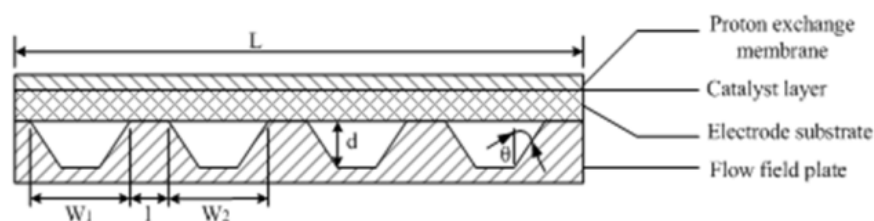
Figure 4.17: Schematic representation of the opening ratio on bipolar plates.

Besides, Figure 4.16 shows that the chamfering angle of opening of micro-flow channels on the specimen still suffered bending force, which limited material movement flowing into channels. To improve this issue, the chamfering angle on the mold was added as a design variable to promote the formability of bipolar plates again. However, considering the practical design, the range of the chamfering angle was approximately 0.1–0.3 mm [15]. Thus, as above mentioned, the design variables, constraints, and object function in the new optimization analysis was listed in Table 4.5. From the new optimization prediction, a group of optimal forming parameters was found and shown in Table 4.6 and Figure 4.18. The predicted channel height reached 0.498 mm with an aspect ratio of 0.539 and the opening ratio on the bipolar plate was up to 54.8%.

Table 4.5: Settings for the new optimization analysis.

features		settings
object function		formed channel aspect ratio
constraints		equivalent strain $\leqq 0.43$
		45% $\leqq$ opening ratio $\leqq$ 75%
design variables	channel width W	0.5 –1.5 mm
	land area S	0.5 –1.5 mm
	draft angle α	14 – 20°
	chamfering angle R	0.1–0.3 mm

Table 4.6: A comparison of 3D optimization prediction and new optimization prediction.

	micro-flow channels on the mold				opening ratio	aspect ratio
	width W	land area S	draft angle α	chamfering angle R		
3D optimization prediction	0.809 mm	1.5 mm	14 °	0.2 mm	35.0%	0.452
new optimization prediction	0.924 mm	0.764 mm	14 °	0.292 mm	54.8%	0.539
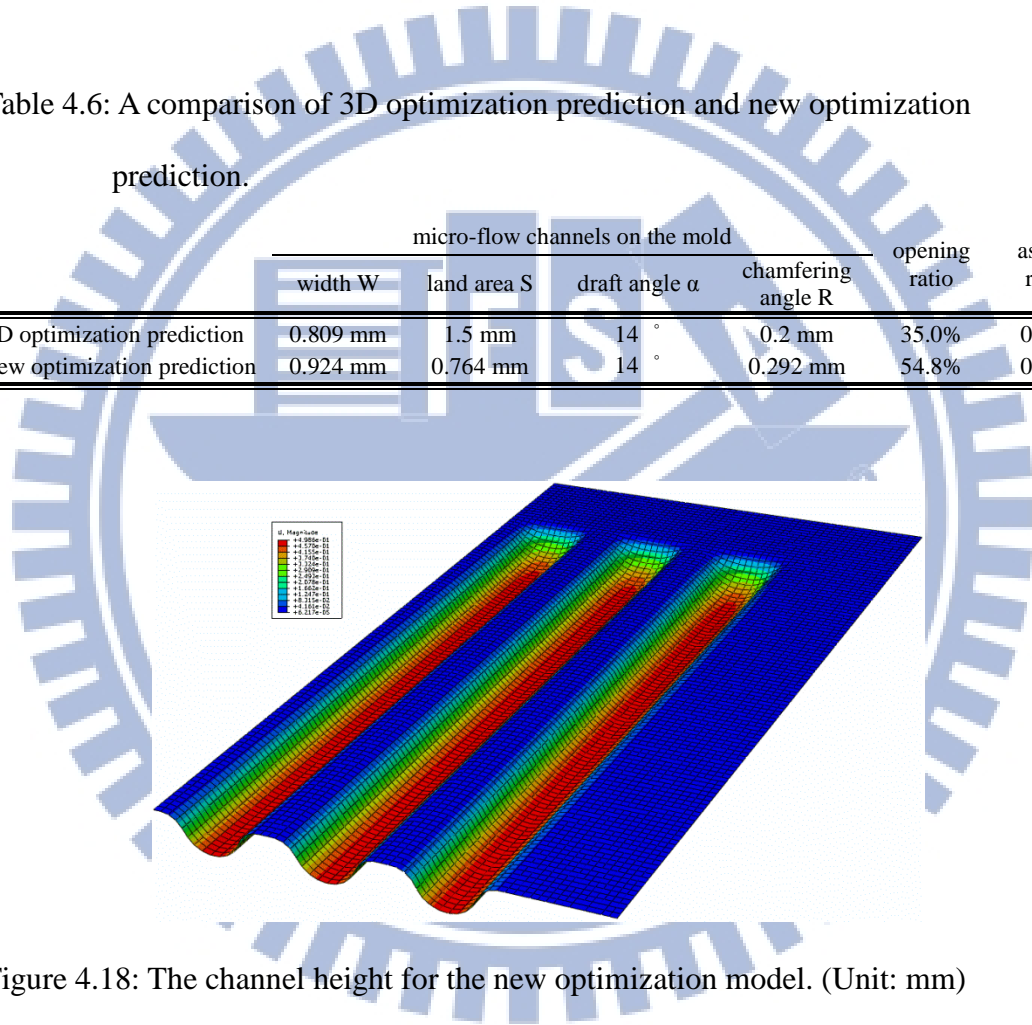
Figure 4.18: The channel height for the new optimization model. (Unit: mm)

The result of the new optimization analysis can act as a reference for designing flow field in a single fuel cell stack; however, in practical applications, a multi-cells fuel cell stack is necessary, and the bottom of channels on the bipolar plates are designed to be flat contact with other bipolar plates (see Figure 4.19) [42]. Therefore, channel geometries in the new optimization prediction with flat bottom channels were finally utilized to act as a reference for designing a multi-cells fuel cell stack. Figure

4.20 shows that channels with flat bottom on the metallic bipolar plates were hydroformed by the developed high-pressure hydroforming process, and the sizes of hydroformed micro channel were 0.924 mm in channel width, 0.765 mm in land area, 14° in draft angle, 0.292 mm in chamfering angle, and 0.39 mm in channel height with an aspect ratio of 0.411.
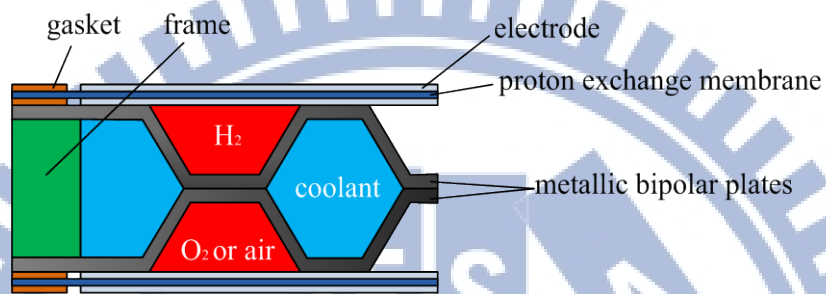

Figure 4.19: Schematic representation of a multi-cells fuel cell stack [42].
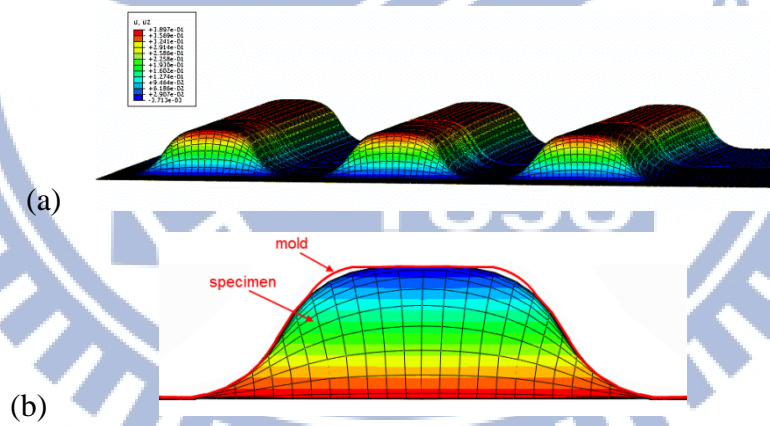

(a)

(b)

Figure 4.20: The new optimization model with flat bottom channels. (Unit: mm)

CHAPTER 5 CONCLUSIONS AND FUTURE WORKS

5.1 Conclusions

In this study, an experimental hydroforming apparatus was designed, built, and modified, with an emphasis on structural simplicity using commercially available materials. A series of experiments was performed to verify the practicability of the apparatus, and satisfactory testing results were obtained with information on the material behavior under various hydrostatic pressures. Several conclusions in this research are offered as follows:

1. The feasibility of this high-pressure hydroforming technique was verified; a two-stage pressure increase structure, a high-pressure container with three tapered layers, and special high-pressure seals were successfully designed and preliminarily proven to safely provide a working pressure of 250 MPa. During the process, the maximum dimensional variation of hydroformed channel heights was approximately 7.48%; therefore, the process control and repeatability of the micro-flow channel hydroforming were reasonably acceptable.

2. Fabrication of the 0.1-mm-thick metallic bipolar plates (SUS304) with the hydroforming apparatus is feasible, and we successfully formed micro-flow channels with an aspect ratio of 0.392. Compared with the maximum aspect ratio of 0.31 formed by the traditional hydroforming process with 0.051 mm thickness SUS304 blanks, the aspect ratio of micro-flow channels in this study was improved by 26.5%, which enabled the fuel cells with metallic bipolar plates to meet both performance and manufacturing requirements. Furthermore, this result also proved that micro-flow channels with a high aspect ratio can be obtained by increasing the forming pressure.

3. The uniformity experiments indicated that the hydroformed micro channels structures were uniform, and no obviously local attenuation condition and no distortion occurred on working area.

4. In the fuel cell performance test, this research confirmed not only the feasibility of hydroformed metallic bipolar plates but also the improvement of the cell performance with increasing channel aspect ratio on bipolar plates.

Simultaneously, to reveal the forming capability of the developed high-pressure hydroforming apparatus, this research constructed the precise 2D and 3D finite element and optimization analyses for this developed high-pressure hydroforming process to attempt to obtain a group of optimal forming parameters and to form an optimal aspect ratio of micro-flow channels on heat treated SUS304 specimens.

The feasibility of the optimization analysis was verified by the follow-up verification experiment, which achieved the channel aspect ratio of 0.411. Compared with the aspect ratio of 0.392 in previous formability experiments, the channel aspect ratio was further increased by 4.8%.

In this research, the forming capability of the developed high-pressure hydroforming technique was revealed through hydroforming experiment, finite element and optimization analyses. Overall, this research developed a complete high-pressure hydroforming technique, which can be applied in forming metallic bipolar plates for portable PEMFCs.

5.2 Future works

1. In this research, the high-pressure hydroforming apparatus with a working area of 40 mm $\times$ 40 mm was successfully developed; however, to widely utilize this high-pressure hydroforming technique, a testing apparatus with a large working area should be further developed.

2. In the follow-up forming process research, a heating device is considered to add to the apparatus. Through this heating device, the formability of specimens should be improved during the process.

3. In the follow-up forming research, the flow field on metallic bipolar plates will be designed according to the new optimization prediction obtained in this research.

4. The developed high-pressure hydroforming technique is attempting to be applied in forming wick structures with high aspect ratio for a flat heat pipe to promote the capability of thermal conduction (see Figures 5.1 and 5.2).
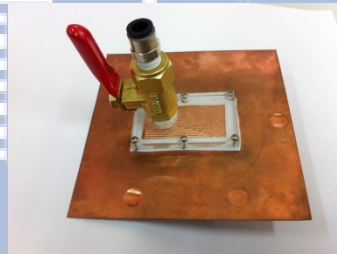
Figure 5.1: Wick structures for a flat heat pipe.
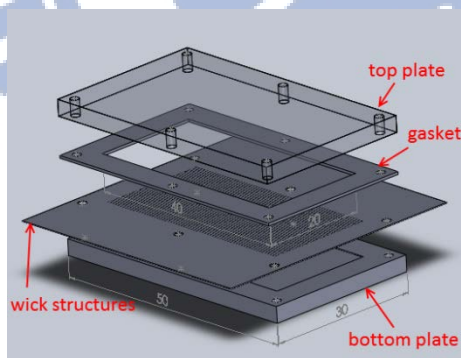
part	specification
top plate	Acrylic Sheet 50*30*5mm
gasket	Copper 50*30*0.5mm
wick structures	Copper C1100 40*40*0.15mm
bottom plate	Copper 50*30*5mm

Figure 5.2: Schematic of a flat heat pipe.

REFERENCES

[1] M. Koc, S. Mahabunphachai," Feasibility investigations on a novel micro-manufacturing process for fabrication of fuel cell bipolar plates: Internal pressure-assisted embossing of micro-channels with in-die mechanical bonding," Journal of Power Sources 178(2007) 725-733.

[2] X. Li, I. Sabir," Review of bipolar plates in PEM fuel cells: Flow-field designs," Journal of Hydrogen Energy 30(2005) 359-371.

[3] E. Middelman, W. Kout, B. Vogelaar, J. Lenssen, E. D. Waal," Bipolar plates for PEM fuel cells: A review," Journal of Power Sources 118(2003) 44–46.

[4] I. Bar-On, R. Kirchain, R. Roth," Technical cost analysis for PEM fuel cells," Journal of Power Sources 109(2002) 71-75.

[5] P. Costamagna, S. Srinivasan," Quantum jumps in the PEMFC science and technology from the 1960s to the year 2000 Part I. Fundamental scientific aspects," Journal of Power Sources 102(2001) 235-269.

[6] H. Tawfik, Y. Hung, D. Mahajan," Metal bipolar plates for PEM fuel cell-A review," Journal of Power Sources 163(2007) 755-767.

[7] S. Mahabunphachai," A hybrid hydroforming and mechanical bonding process for fuel cell bipolar plates," A dissertation of Doctor of Philosophy (Mechanical Engineering), The University of Michigan, 2008.

[8] Taiwan Fuel Cell information website. http://www.tfci.org.tw.

[9] X. Li, I. Sabir," Review of bipolar plates in PEM fuel cells: Flow-field designs," Journal of Hydrogen Energy 30(2005) 359-371.

[10] E. Middelman, W. Kout, B. Vogelaar, J. Lenssen, E. D. Waal," Bipolar plates for PEM fuel cells: A review," Journal of Power Sources 118(2003) 44–46.

[11] E. A. Cho, U. S. Jeon, H. Y. Ha, S. A. Hong, I. H. Oh," Characteristics of

composite bipolar plates for polymer. Electrolyte membrane fuel cells," Journal of Power Sources 125(2004) 178–182.

[12] A. P. Manso, F. F. Marzo, M. G. Mujika, J. Barranco, A. Lorenzo," Numerical analysis of the influence of the channel cross-section aspect ratio on the performance of a PEM fuel cell with serpentine flow field design," Journal of Hydrogen Energy 36(2011) 6795-6808.

[13] J. C. Hung, T. C. Yang, K. C. Li," Studies on the fabrication of metallic bipolar plates—Using micro electrical discharge machining milling," Journal of Power Sources 196(2011) 2070-2074.

[14] S. J. Lee, C. Y. Lee," Simulation and fabrication of micro-scaled flow channels for metallic bipolar plates by the electrochemical micro-machining process," Journal of Power Sources 185(2008) 1115–1121.

[15] Y. Liu, L. Hu," Fabrication of metallic bipolar plate for proton exchange membrane fuel cells by rubber pad forming," Journal of Power Sources 195(2010) 3529–3535.

[16] Y. Liu, L. Hua, J. Lan, X. Wei," Studies of the deformation styles of the rubber-pad forming process used for manufacturing metallic bipolar plates," Journal of Power Sources 195(2010) 8177–8184.

[17] S. Mahabunphachai, O. N. Cora, M. Koc," Effect of manufacturing processes on formability and surface topography of proton exchange membrane fuel cell metallic bipolar plates," Journal of Power Sources 195(2010) 5269–5277.

[18] S. Mahabunphachai, M. Koc," Fabrication of micro-channel arrays on thin metallic sheet using internal fluid pressure: Investigations on size effects and development of design guidelines," Journal of Power Sources 175(2008) 363–371.

[19] S. Masatoshi, N. Katsuyuki," Processing method, magnetic transfer method and

recording medium," Japan Patent, JP2003-157520 (2003).

[20] L. Olsson," Imprint method and device," United States Patent, US20030189273 (2003).

[21] J. J. Lee," Imprinting apparatus for forming pattern at uniform contact by additional constant," World Intellectual Property Organization Patent, WO2006135170 (2006).

[22] T. Ando, S. Komoriya, M. Ogino, C. Haginoya, A. Mitauchi," Imprinting device and microstructure transfer method," United States Patent, US20060286193 (2006).

[23] J. C. Hung, C. H. Hung," uniform pressing apparatus for use in a micro-nano imprint process," United States Patent, US7462029 (2008).

[24] A. Hermann, T. Chaudhuri, P. Spagnol," Bipolar plates for PEM fuel cells:A review," Journal of Hydrogen Energy 30(2005) 1297-1302.

[25] B. Cunningham, D. G. Baird," The Development of Economical Bipolar Plates for Fuel Cells," Journal of Material Chemistry 16(2006) 4385–4388.

[26] J. Wind, R. Spah, W. Kaiser, G. Boehm," Metallic bipolar plates for PEM. fuel cells," Journal of Power Sources 105(2002) 256–260.

[27] J. P. Allen," Bipolar Separator and Current Collector Design and. Manufacture," 2000 Fuel Cell Seminar Abstracts (2000) 55–58.

[28] M. C. Li, C. L. Zeng, S. Z. Luo, J. N. Shen, H. C. Lin, C. N. Cao," Electrochemical corrosion characteristics of type 316 stainless steel in simulated anode environment for PEMFC," Electrochimica Acta 48(2003) 1735–1741.

[29] F. Dundar, E. Dur, S. Mahabunphachai, M. Koc," Corrosion resistance characteristics of stamped and hydroformed proton exchange membrane fuel cell metallic bipolar plates," Journal of Power Sources 195(2010) 3546–3552.

[30] J. C. Hung, C. Hung," The design and development of a hydrostatic extrusion

apparatus," Journal of Materials Processing Technology 104(2000) 226-235.

[31] S. Timoshenko," Strength of Materials, Part II," D. Van Nostrand Co., Princeton, N. J., 1930.

[32] H. L. D. Pugh," Recent Developments in Cold Forming," Bullied Memorial Lectures, Vol. III, University of Nottingham, 1965.

[33] S. J. Becker, L. Mollick," Theory of Ideal Design of a Compound Vessel," ASME. Journal of Engineering for Industry, 1960.

[34] S. J. Becker," Analysis of a Yielded Compound Cylinder," ASME. Journal of Engineering for Industry, 83(1961) 43.

[35] S. J. Becker," Yielded Compound Cylinder in Generalised Plane Strain," ASME. Journal of Engineering for Industry, 83(1961) 441.

[36] T. E. Davidon, D. P. Kendall," The design of high pressure containers and associated equipment," in: H. L. D. Pugh (Eds.), Mechanical behavior of materials under pressure, Elsevier publishing Co., New York, 1970.

[37] P. W. Bridgman," The Physics of High Pressure," Bell, London, 1931.

[38] E. Whalley, A. Lavergne," Modified unsupported-area hydraulic seal for pressure of 50 kilobar," Review of Scientific Instruments 47 (1976) 136-137.

[39] L. Peng, X. Lai, D. Liu, P. Hua, J. Ni," Flow channel shape optimum design for hydroformed metal bipolar plate in PEM fuel cell," Journal of Power Sources 178(2008) 223-230.

[40] SmartDO. http://www.smartdo.co/index_e.htm.

[41] Z. Marciniak, J. L. Duncan, S. J. Hu," Mechanics of Sheet Metal Forming," Second edition, Butterworth-Heinemann, 2002.

[42] C. C. Huang, " fuel cells," Tsang hai book publishing Co., Taichung, third version, 2008 (traditional Chinese).

Appendix A: The designs of hydroforming apparatus

A.1 A servo hydrostatic pressing machine

A novel high-pressure hydroforming apparatus (Figure 2.2) was designed and constructed including a high-pressure source, a servo hydrostatic pressing machine with a maximum capacity of 100 tons. There is one main cylinder and four slave cylinders in the machine (see Figure A.1). During hydroforming, four slave cylinders pushed the platform and pressure container to contact the mold and offered holding force to seal the working area. Main cylinder offered 100 tons axial force to push the primary plunger, and fluid pressure was produced in the high-pressure container.

(a)
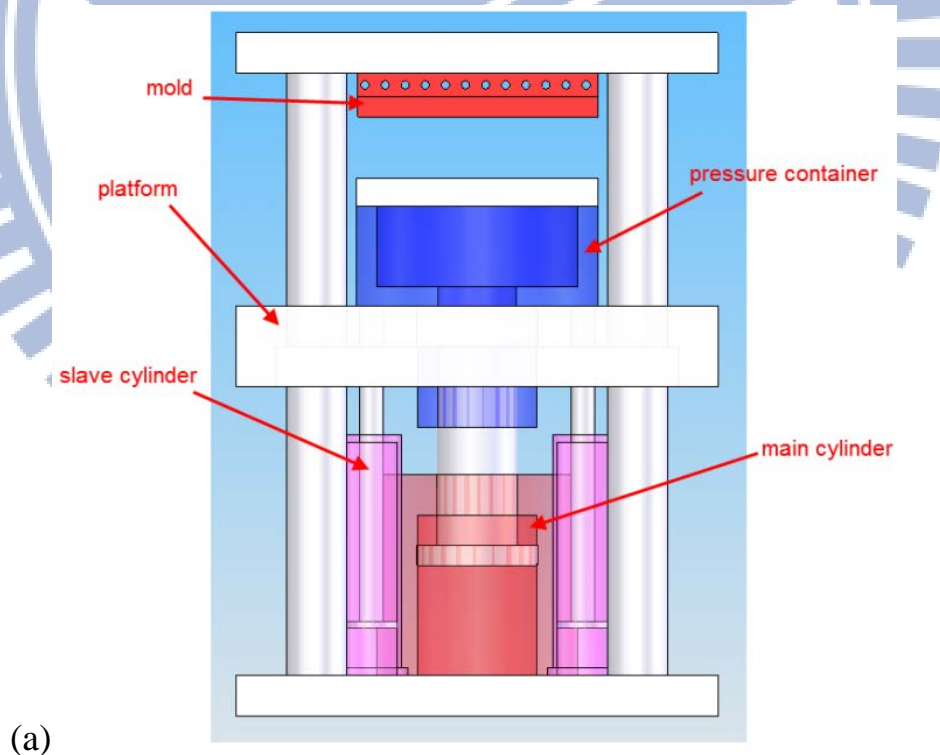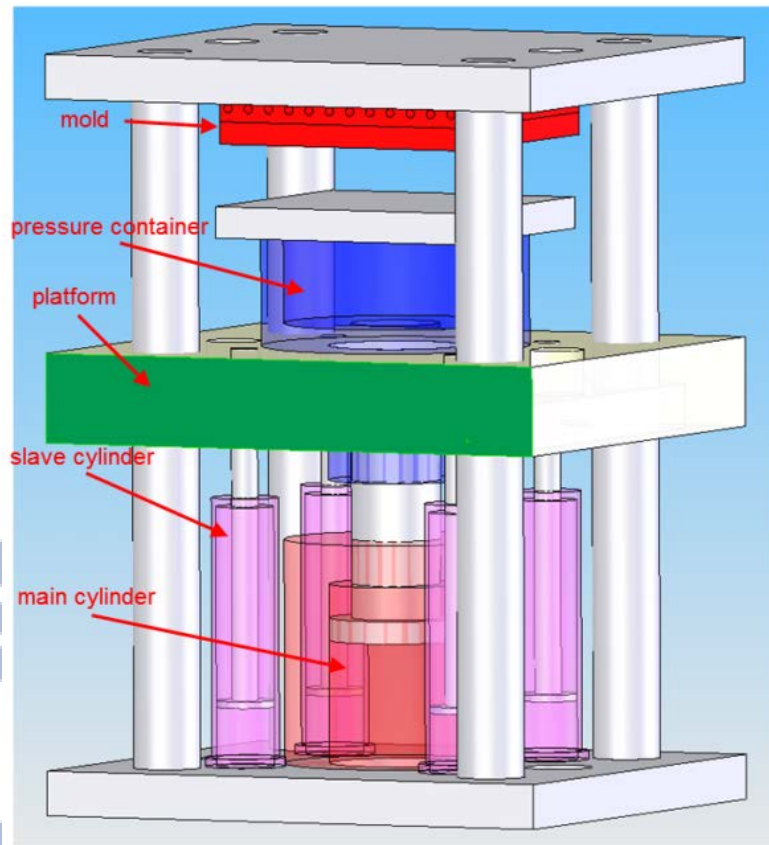
(b)

Figure A.1: Schematic representation of a servo hydrostatic pressing machine.

A.2 Pressure measurement

The high-pressure container was constructed using a three-layer cylinder which cannot drill a hole in the container. Thus, fluid pressure in the container was not measured directly using a manometer. To solve this issue, this study developed an indirect pressure measurement approach. A load cell was set in the upper shell (see Figure A.2a). When being worked on the mold, fluid pressure was also transmitted to the load cell through the mold (see Figure A.2). Although friction force existed between the mold and clamping apparatus affecting the pressure transmission, friction force was neglected because fluid pressure was extremely higher than it.
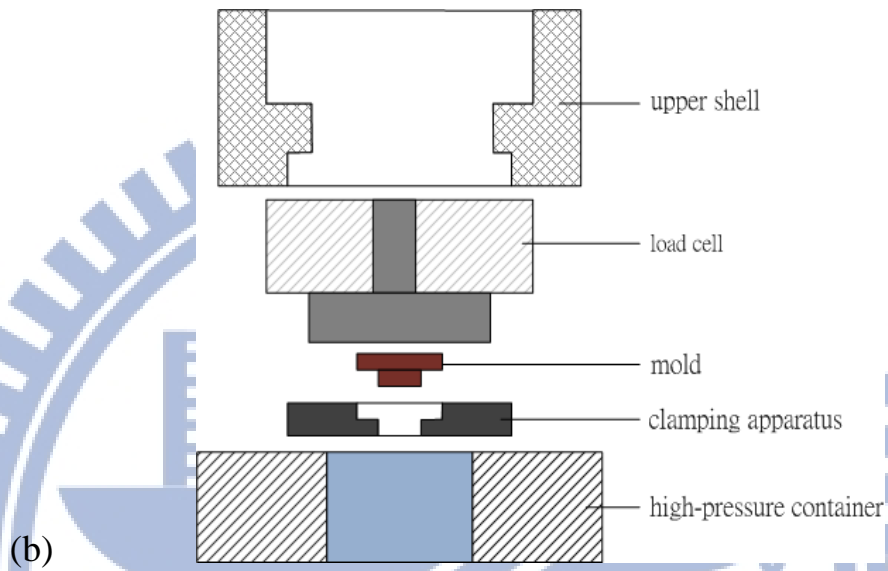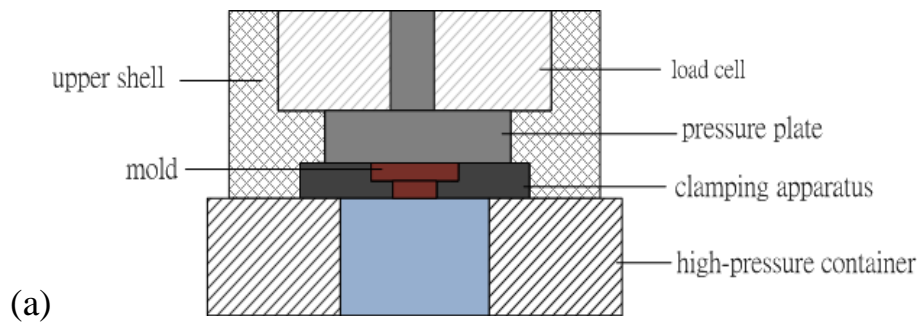
Figure A.2: An indirect pressure measurement device.

Appendix B: Metallographic test

The specimens receiving the solution heat treatment were observed metallographic ally, and the procedure of the test is as follow:

1. The specimen is embedded with PhenoCure®.

2. The surface of the specimen is grinded by sand paper using different particle sizes of 240, 400, 600, 800, 1000, 1200, 1500 in turn. The direction of the next particle size grinding needs to rotate 90 degree of the direction of the last particle size grinding, and the grinding crack of the last particle size grinding need to be removed.

3. The grinded specimen is polished by a polishing machine using $1\mu m$ particle size alumina solution.

4. After polishing, the specimen is cleaned by water and then dried. Subsequently, the specimen is corroded using an etchant according to ASTM E407–70 (Table B.1). Samples are etched for approximately 15–20 seconds to expose the grain boundary on the surface of samples. After etching, samples can be observed and captured the image by an optical microscope.

Table B.1: The composition of an etchant.

composition	percentage (%)
HNO_3	50
HCl	25
H_2O	25

Average grain sizes of heat treatment blanks were measured according to the ASTM Standard E112-88 (mean lineal intercept or Heyn's method). Several lines including 45 degree oblique, horizontal, and vertical lines were drawn on the images

captured from an optical microscope, and the numbers of grains intercepted in lines were measured. Hence, average grain sizes were calculated as follows:

$$D = \left(\frac{L}{N}\right) \times \left(\frac{1}{M}\right) \qquad (B.1)$$

where D is average grain sizes, L is total length of lines drawn in the image, N is the numbers of intercepted grains, and M is a magnification factor from an optical microscope.

The metallographic structure of heat treated SUS304 specimens with 0.1 mm thickness was captured by a microscope shown in Figure B.1. Average grain size calculated from Eq. B.1 was approximately $43.86\,\mu m$.
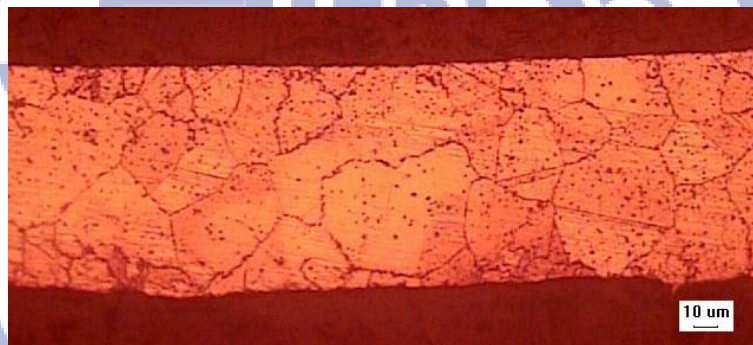
Figure B.1: The metallographic structure of heat treated SUS304 specimens.

Appendix C: Forming limit test

C.1 The principle of forming limit diagram (FLD)

In the forming limit diagram (FLD), the longitudinal axis shows major strain while the horizontal axis shows minor strain, and the sheet strain obtained from every type of forming to fracture were drawn in the figure (Figure C.1). The curve in FLD is like a ribbon region. In the figure, if the strain data composed of ε_1 and ε_2 is beyond the ribbon, the specimen is broken; if the data is below the ribbon, the specimen is safe; however, if the data is located in the ribbon, the specimen has the risk of fracture.
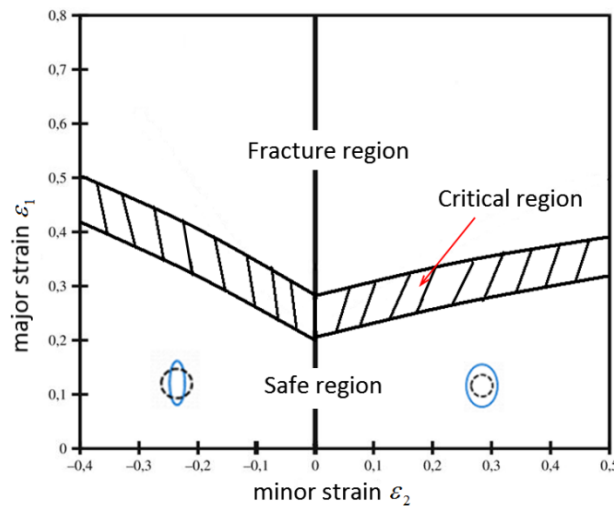
Figure C.1: Schematic of the forming limit diagram (FLD).

FLD is a principle estimating sheet formability. Different types of strain conditions will be gained from sheet forming under different types of stress conditions. Furthermore, FLD not only has different types of strain data but also includes the extreme strain data when sheet fracture and a circle grid analysis is an approach to comprehend the strain conditions after sheet forming.

First, circle grids are uniformly etched on metallic blanks, and then the deformed circle grids are observed after sheet forming. The original grid diameter is d_0, and the grids are deformed into different diameters d_1 and d_2 when blanks receive a plane strain, as shown in Figure C.2. The strain amount could be measured through changes on grids, the major stain of which is $\varepsilon_1 = \ln(d_1/d_0)$ and the minor stain of which is $\varepsilon_2 = \ln(d_2/d_0)$. Finally, sheet forming conditions could be understood.
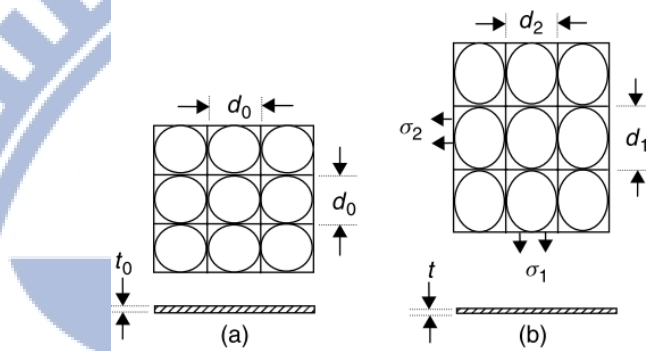
Figure C.2: An element of a sheet showing: (a) the undeformed state with circle and square grids marked on it; (b) the deformed state with the grid circles deformed to ellipses of major diameter d_1 and minor diameter d_2 [41].

The individual points on the strain locus in Figure C.3c can be obtained from measurements of a grid circles as shown in Figure C.2. It is usual to assume that the strain path is linear, i.e. the strain ratio remains constant and is given by

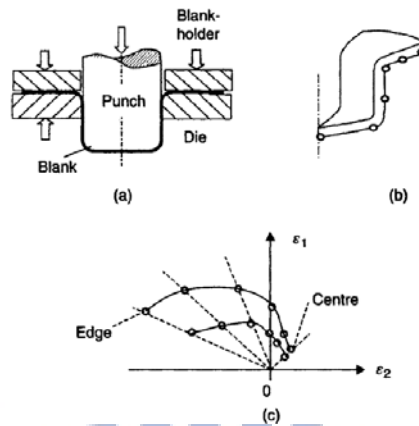$$\beta = \frac{\varepsilon_2}{\varepsilon_1} = \frac{\ln(d_2/d_0)}{\ln(d_1/d_0)}$$

Figure C.3: (a) Deep drawing a cylindrical cup. (b) Sector of a cup showing the location of strain measurements. (c) Strain plots for two stages in the drawing process [41].

FLD shows different deformation types through different strain paths, i.e. equal biaxial stretching ($\beta = 1$), plane strain ($\beta = 0$), uniaxial tension ($\beta = -1/2$), pure shear ($\beta = -1$), and uniaxial compression ($\beta = -2$), as shown in Figures C.4a–g.
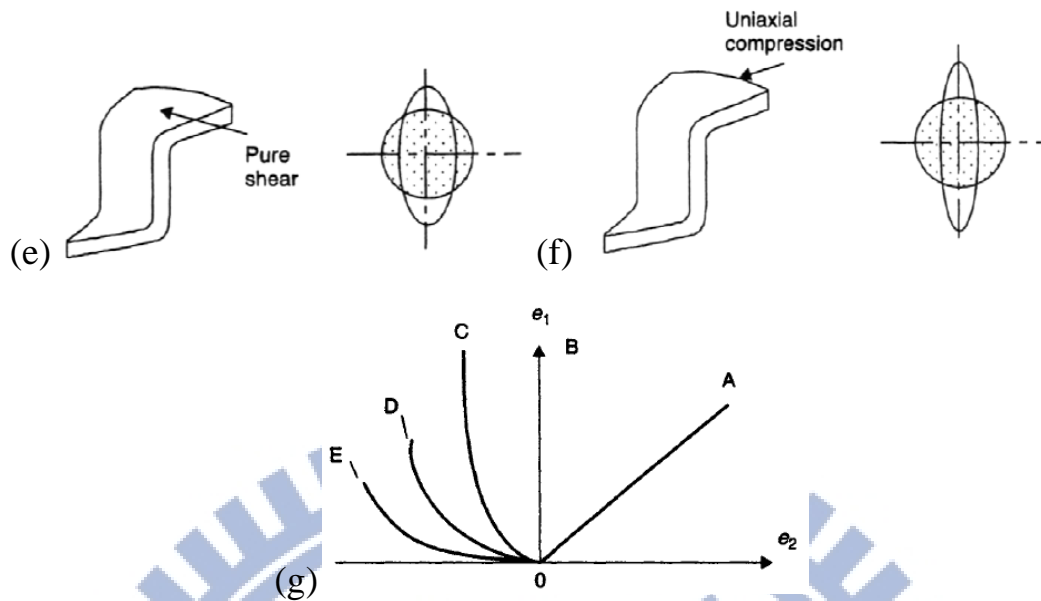

(a)

(b)

(c)

(d)

(e) (f)

(g)
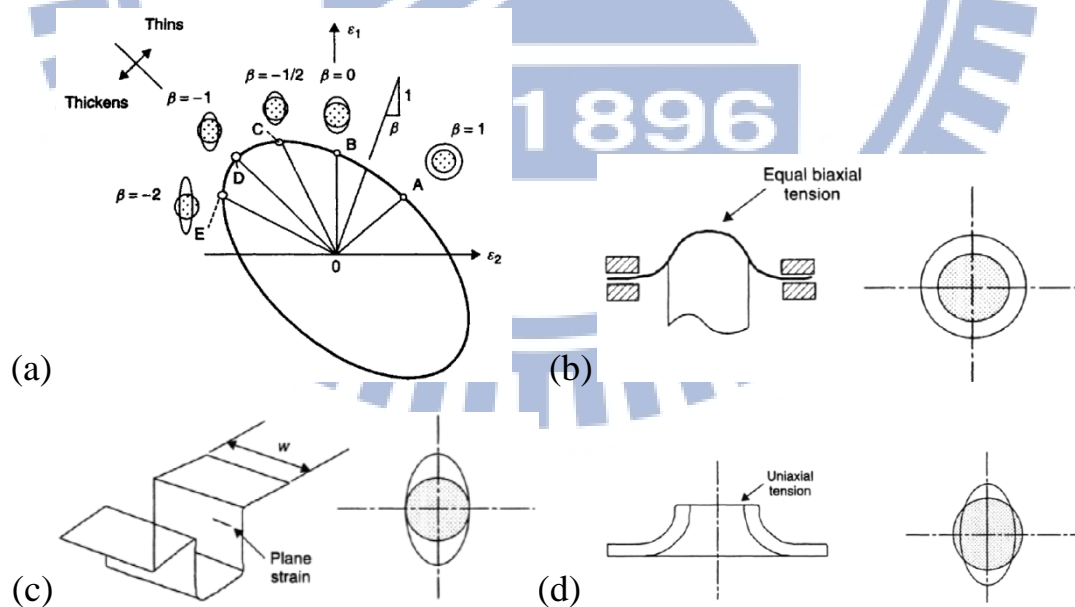
Figure C.4: (a) The strain diagram showing the different deformation modes corresponding to different strain ratios. (b) Equibiaxial stretching at the pole of a stretched dome. (c) Deformation in plane strain in the side-wail of a long part. (d) Uniaxial extension of the edge of an extruded hole. (e) Drawing or pure shear in the flange of a deep-drawn cup, showing a grid circle expanding in one direction and contracting in the other. (f) Uniaxial compression at the edge of a deep-drawn cup. (g) The different proportional strain paths shown in Figure C.3 plotted in an engineering strain diagram [41].

C.2 Forming limit experiments

To investigate and understand the forming limit and procedure of sheet forming, forming limit test was conducted, and the forming limit diagram (FLD) was derived by the test.

50 ton universal deep drawing testing machine (SAS-50-D, TOKYO TESTING MACHINE INC.) was utilized in this research (Figure C.5). The mold and punch are

73

shown in Figure C.6, and the diameter of the punch is 60 mm. Heat treated SUS304 specimens with a dimension of $100 \times 100 \times 0.1$ mm were used and changed into different shapes (Figure C.7) to obtain different strain paths. Simultaneously, circle grids with a diameter of 5 mm were uniformly etched on the thin blanks, as shown in Figure C.8.

Figure C.5: Universal deep drawing testing machine.

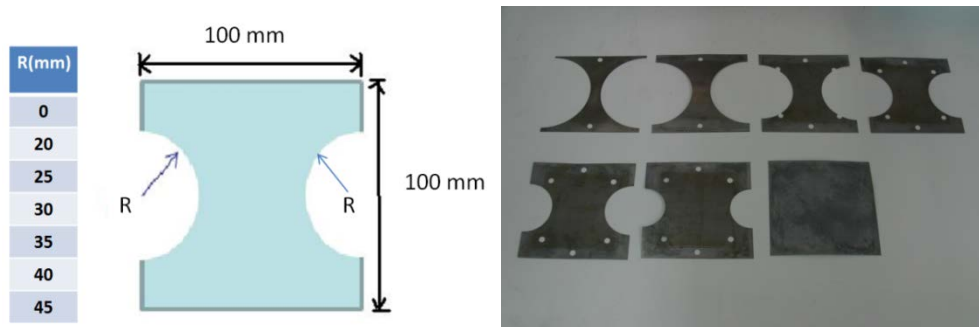
Figure C.6: The mold and punch of a universal deep drawing testing machine.

Figure C.7: Different shapes of SUS304 specimens.
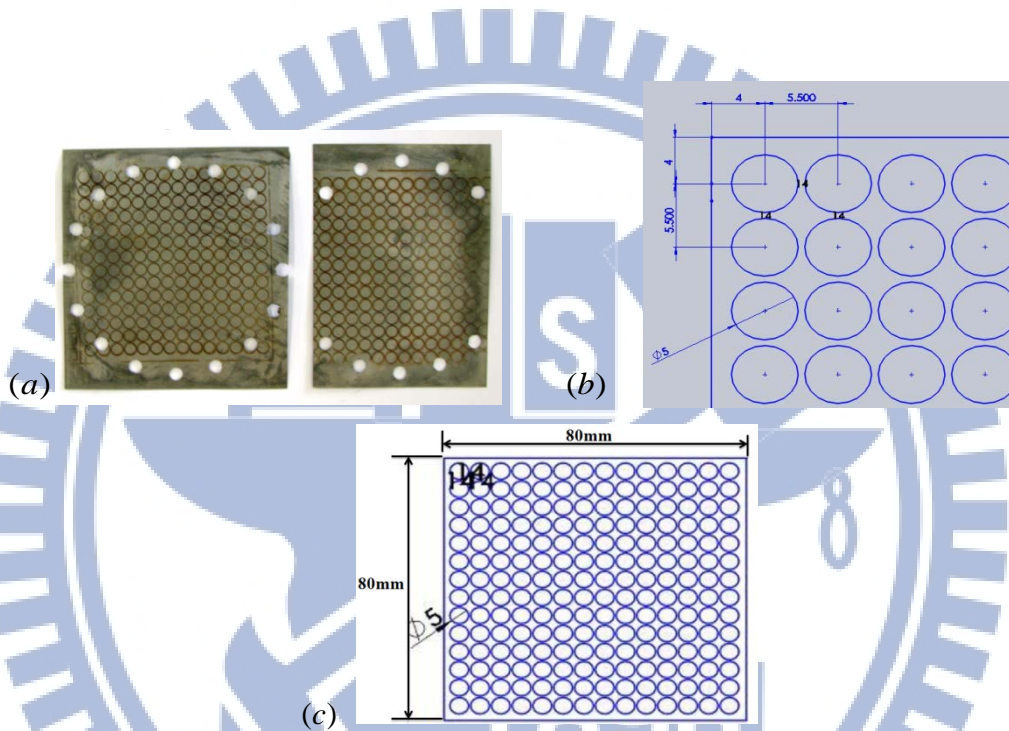
Figure C.8: Circle grids with a diameter of 5 mm etched on heat treated SUS304 specimens.

Samples after the test are shown in Figure C.9. The forming limit strain was calculated by observing changes on circle grids of thin blanks, and the forming limit diagram was drawn (Figure C.10).

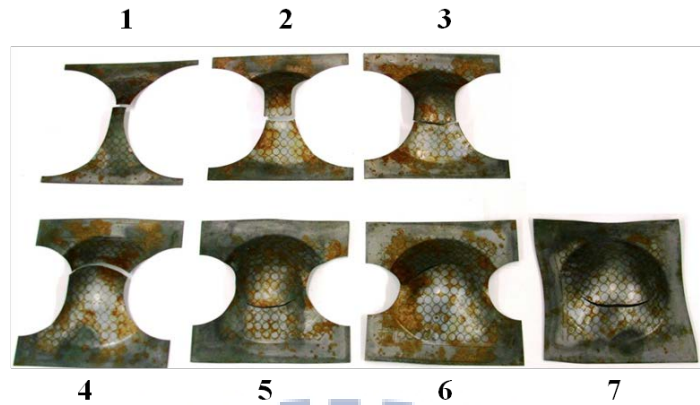Figure C.9: Samples after a forming limit test.

In Figure C.9, specimen No. 7 was designed to simulate strain path of equal biaxial tension condition (Figure C.4b), the data of which were located on the right side of FLD theoretically. However, specimen No.7 could not be clamped firm because of extremely thin thickness of 0.1 mm, and the contact pressure between specimen No. 7 and the punch was greater than the holding force which the testing machine could offer. Therefore, after the test, specimen No. 7 shown in Figure C.9 had the indentation condition on the edges of the specimen, which was different from the ideal deformation type. Finally, the data derived from specimen No. 7 was located on the vertical axial representing plane strain condition (Figure C.10), and FLD derived from the forming limit test lacked the data on the right side.
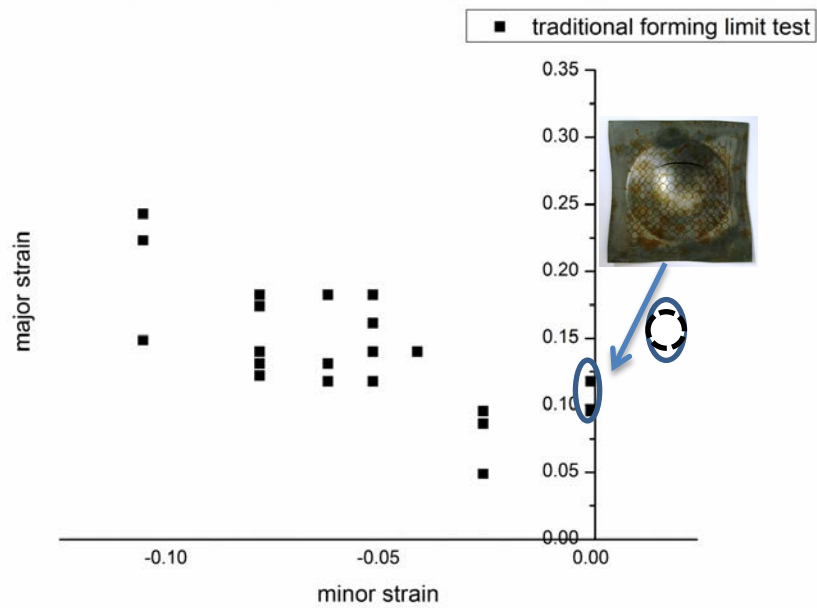
Figure C.10: FLD for heat treated SUS304 specimens.

To overcome this issue, a novel hydraulic measuring apparatus was designed (Figures C.11), and samples in Figure C.7 were utilized in this device.
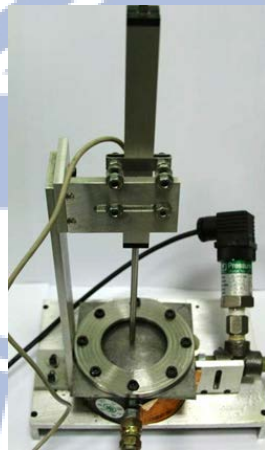

Figure C.11: a novel hydraulic measuring apparatus.

In this measuring apparatus, a rubber layer is utilized and acts as a flexible punch. During the experiment, R68 oil as working fluid is injected into the lower die and provides fluid pressure, which can deform a rubber layer and then form a specimen. Through this design, the volume of a testing apparatus can be reduced, and a holding

force can be offered by numbers of screws. Besides, this measuring apparatus also can do the bulging test for thin metallic blanks to acquire the true stress-strain curve of a material. This novel hydraulic measuring apparatus combined with forming limit test and bulging test for thin metallic blanks is applying for a US patent.
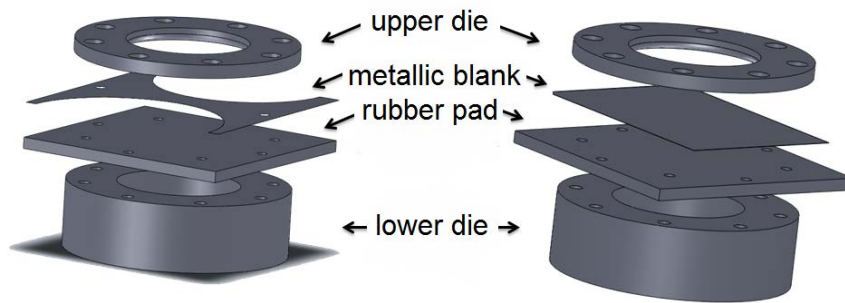

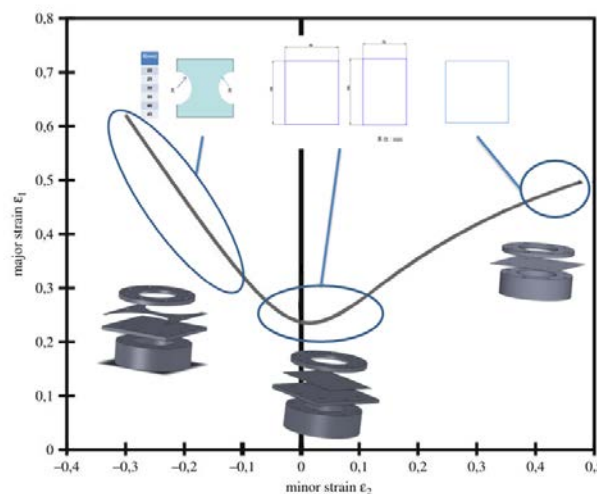Figure C.12: the components of a novel hydraulic measuring apparatus.

Figure C.13: Schematic representation of a novel hydraulic measuring apparatus.

From the experiment result (Figure C.14), the data derived from the new measuring apparatus had the similar tendency to those obtained from a tradition forming limit test, which confirmed the feasibility of this new design, and the data on the right side of FLD was gained (Figure C.14). Finally, FLD data of heat treated SUS304 specimens was obtained completely.
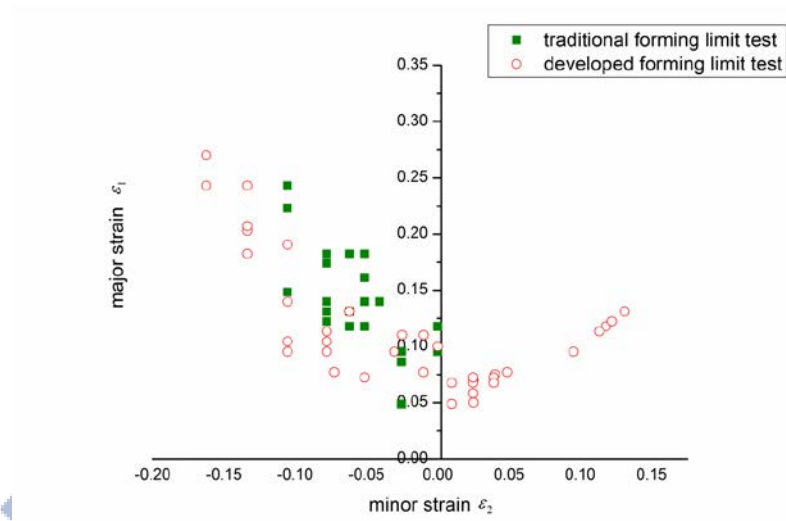
Figure C.14: A comparison of traditional and developed forming limit tests.